

The electron-capture origin of supernova 2018zd

Daichi Hiramatsu^{1,2*}, D. Andrew Howell^{1,2}, Schuyler D. Van Dyk³, Jared A. Goldberg², Keiichi Maeda^{4,5}, Takashi J. Moriya^{6,7}, Nozomu Tominaga^{8,5}, Ken'ichi Nomoto⁵, Griffin Hosseinzadeh⁹, Iair Arcavi^{10,11}, Curtis McCully^{1,2}, Jamison Burke^{1,2}, K. Azalee Bostroem¹², Stefano Valenti¹², Yize Dong¹², Peter J. Brown¹³, Jennifer E. Andrews¹⁴, Christopher Bilinski¹⁴, G. Grant Williams^{14,15}, Paul S. Smith¹⁴, Nathan Smith¹⁴, David J. Sand¹⁴, Gagandeep S. Anand^{16,17}, Chengyuan Xu¹⁸, Alexei V. Filippenko^{19,20}, Melina C. Bersten^{21,22,5}, Gastón Folatelli^{21,22,5}, Patrick L. Kelly²³, Toshihide Noguchi²⁴ & Koichi Itagaki²⁵

*Corresponding author. Email: dhiramatsu@lco.global

¹*Las Cumbres Observatory, 6740 Cortona Drive, Suite 102, Goleta, CA 93117-5575, USA*

²*Department of Physics, University of California, Santa Barbara, CA 93106-9530, USA*

³*Caltech/Spitzer Science Center, Caltech/IPAC, Mailcode 100-22, Pasadena, CA 91125, USA*

⁴*Department of Astronomy, Kyoto University, Kitashirakawa-Oiwake-cho, Sakyo-ku, Kyoto 606-8502, Japan*

⁵*Kavli Institute for the Physics and Mathematics of the Universe (WPI), The University of Tokyo Institutes for Advanced Study, The University of Tokyo, 5-1-5 Kashiwanoha, Kashiwa, Chiba 277-8583, Japan*

⁶*National Astronomical Observatory of Japan, National Institutes of Natural Sciences, 2-21-1 Osawa, Mitaka, Tokyo 181-8588, Japan*

⁷*School of Physics and Astronomy, Faculty of Science, Monash University, Clayton, Victoria*

3800, Australia

⁸*Department of Physics, Faculty of Science and Engineering, Konan University, 8-9-1 Okamoto, Kobe, Hyogo 658-8501, Japan*

⁹*Center for Astrophysics | Harvard & Smithsonian, 60 Garden Street, Cambridge, MA 02138-1516, USA*

¹⁰*The School of Physics and Astronomy, Tel Aviv University, Tel Aviv 69978, Israel*

¹¹*CIFAR Azrieli Global Scholars program, CIFAR, Toronto, Canada*

¹²*Department of Physics, University of California, 1 Shields Ave, Davis, CA 95616-5270, USA*

¹³*Mitchell Institute for Fundamental Physics and Astronomy, Texas A&M University, College Station, TX 77843, USA*

¹⁴*Steward Observatory, University of Arizona, 933 North Cherry Avenue, Tucson, AZ 85721-0065, USA*

¹⁵*MMT Observatory, P.O. Box 210065, Tucson, AZ 85721-0065, USA*

¹⁶*Infrared Processing and Analysis Center, California Institute of Technology, Pasadena, CA 91125, USA*

¹⁷*Institute for Astronomy, University of Hawai'i, 2680 Woodlawn Drive, Honolulu, HI 96822, USA*

¹⁸*Media Arts and Technology, University of California, Santa Barbara, CA 93106-6065, USA*

¹⁹*Department of Astronomy, University of California, Berkeley, CA 94720-3411, USA*

²⁰*Miller Senior Fellow, Miller Institute for Basic Research in Science, University of California, Berkeley, CA 94720, USA*

²¹*Instituto de Astrofísica de La Plata (IALP), CONICET, Argentina*

²²*Facultad de Ciencias Astronómicas y Geofísicas, Universidad Nacional de La Plata, Paseo del Bosque, B1900FWA, La Plata, Argentina*

²³*School of Physics and Astronomy, University of Minnesota, 116 Church Street SE, Minneapolis, MN 55455, USA*

²⁴*Noguchi Astronomical Observatory, Katori, Chiba 287-0011, Japan*

²⁵*Itagaki Astronomical Observatory, Yamagata, Yamagata 990-2492, Japan*

There are two well-understood regimes of stellar death, although the transition has remained unresolved for 40 years. Stars up to about 8 solar masses lose their outer layers and leave behind a degenerate core – a white dwarf. More massive stars (above ~ 10 solar masses) produce an iron core, which collapse to a neutron star or black hole in a core-collapse supernova. Theoretically, stars in between ($\sim 8\text{--}10$ solar masses) are expected to produce an electron-capture supernova when the degenerate O+Ne+Mg core of a super-asymptotic giant branch star collapses as a result of electron capture onto Ne and Mg nuclei^{1, 2, 3}. However, until now no supernovae have unequivocally been identified from an electron-capture origin, partly because of uncertainty in theoretical predictions. Here we present six indicators of electron-capture supernovae: progenitor identification, circumstellar material, chemical composition^{4, 5, 6}, explosion energy, light curve, and nucleosynthesis^{7, 8, 9, 10, 11}. SN 2018zd is the only supernova having strong evidence for or consistent with all six. These new data cast the decades-long debate about SN 1054 in a new light, which has some of these characteristics, but suffers from thousand year old observations and the difficulty of making inferences from evolved supernova remnants.

On 2018 Mar. 2.49 (UT dates are used throughout), we discovered AT 2018zd¹² at an unfiltered optical magnitude of 17.8 in the outskirts of NGC 2146 (redshift $z = 0.002979$ ¹³), where pre-explosion *Hubble Space Telescope* (*HST*) and *Spitzer Space Telescope* images yield a faint progenitor candidate (Extended Data Figs. 1 & 2, and Methods). Combined with our pre-discovery detection at 18.1 mag on 2018 Mar. 1.54, we estimate an explosion epoch of 2018 Mar. 1.4 ± 0.1 (~ 3 hr before the first detection; Extended Data Fig. 3 and Methods) and use it as a reference

epoch for all phases. At 4.9 days post explosion, we classified AT 2018zd as a young Type II (hydrogen-rich) supernova (SN), designating it SN 2018zd¹⁴. Over time, SN 2018zd developed a plateau and broad Balmer-series P-Cygni lines in the optical light curve and spectra, respectively, further classifying it as a Type II-P (plateau) SN (Extended Data Figs. 3 & 4). The luminosity distance of NGC 2146 is uncertain, ranging from 11 to 18 Mpc in the literature¹⁵. Thus, we apply the standard candle method and adopt a distance of 9.6 ± 1.0 Mpc (see Methods). Because of the wide distance range, we focus mainly on distance-independent measurements.

Unlike Fe core-collapse (CC) SN explosions of red supergiant (RSG) stars, electron-capture (EC) SN explosions of super-asymptotic giant branch (SAGB) stars are robustly realised by first-principle simulations, facilitated by the steep density gradient outside the degenerate core. Simulations consistently predict explosion energy ($\sim 2 \times 10^{50}$ erg) and ⁵⁶Ni yield ($\sim 3 \times 10^{-3} M_{\odot}$ with an upper limit $\lesssim 10^{-2} M_{\odot}$) that are an order-of-magnitude lower than those observed for typical Fe CCSNe^{7, 8, 10}, but are consistent within the lowest-mass Fe CCSNe (see Methods). Despite the low explosion energy, the low mass and large radius of an SAGB star result in a light-curve morphology virtually identical to that of Type II-P SNe, except for a larger drop (~ 4 mag) from the plateau to the radioactive decay tail, due to the low ⁵⁶Ni production⁹.

Among a sample of well-observed Type II SN light curves¹⁶ (Fig. 1), SN 2018zd fits in the Type II-P morphology and displays the largest plateau drop (~ 3.8 mag). Even among a sample of low-luminosity Type II-P SNe¹⁷ that often show larger plateau drops than other Type II subclasses (Fig. 1), SN 2018zd is comparable to SNe 1999eu and 2006ov with the largest drops

ever observed, which indicates an intrinsically low ^{56}Ni production. For SNe 1999eu and 2006ov, the lack of additional data prevents the investigations of other ECSN indicators, and the light curves alone cannot be conclusive evidence (see Methods for the light-curve degeneracy). The tail decline rate of SN 2018zd is consistent with the ^{56}Co heating rate, and an estimated ^{56}Ni mass is $(8.6 \pm 0.5) \times 10^{-3} M_{\odot}$ at the assumed luminosity distance of 9.6 Mpc (Extended Data Fig. 3). This is larger than the canonical ^{56}Ni yield for ECSNe, but still within the upper limit (see also Methods for the effect of distance uncertainty).

As SAGB stars are thought to have mass-loss rates ($\dot{M} \approx 10^{-4} M_{\odot} \text{ yr}^{-1}$) a few orders of magnitude higher than those of RSG stars of similar initial mass⁴, the circumstellar material (CSM) density is expected to be a few orders of magnitude higher, as it scales as $\rho_{\text{CSM}} \propto \dot{M}/v_{\text{wind}}$, assuming constant wind mass loss with similar SAGB and RSG wind velocities¹⁸ v_{wind} . Compared to RSG stars, the CSM composition of SAGB stars can be He-, C-, and N-rich, but O-poor, depending on the efficiency of the SAGB dredge-up/out that bring the partial H- and He-burning products to the stellar surface^{5,6}.

In a sample of Type II SN ultraviolet (UV) colours¹⁶, SN 2018zd stands out, reaching the minimum in $U - V$ colour (i.e., becoming bluer until) ~ 5 d after the explosion (Fig. 2), which suggests a possible delayed shock-breakout through dense CSM¹⁹. In such a case, a photosphere initially forms inside the unshocked optically-thick CSM²⁰; this provides an additional power source leading to the bluer colour when the shock front is propagating through the CSM (see Extended Data Fig. 5 for the same effect on the photospheric velocity). Our MESA+STELLA CSM light-

curve models (see Methods and Extended Data Fig. 6) show that $\dot{M} \approx 0.01 M_{\odot} \text{ yr}^{-1}$ for the last ~ 10 yr before the explosion is required to reproduce the early-time $U - V$ colour of SN 2018zd, assuming a typical constant¹⁸ $v_{\text{wind}} = 20 \text{ km s}^{-1}$ (Fig. 2). Since the estimated mass loss is a few orders of magnitude greater than that expected from SAGB or RSG wind, it is likely dominated by eruptive events^{4,5}.

Consistent with the possible delayed shock breakout seen in the early UV colour, SN 2018zd exhibits unusually persistent ($\gtrsim 9$ d) flash features, reaching the highest ionisation states at ~ 5 d after the explosion (Fig. 3). The strengths of flash features depend on the photospheric temperature, CSM density, and CSM abundance^{21,22,23}. We constrain the photospheric temperature and CSM density of SN 2018zd by the MESA+STELLA UV-colour models. Then we use emission-line intensity ratios as diagnostics of CSM abundance by comparing with the flash spectral models of solar-abundance and He-rich atmospheres²² (Fig. 3; note that the line ratios are not well reproduced by either solar-abundance or He-rich models alone²³, and a mixture of both with higher density needs to be modeled for a more detailed abundance analysis). Based on the model comparisons, we estimate He-, C-, and N-rich, but O-poor CSM mass fractions of $X_{\text{He}} \approx 0.3\text{--}0.8$, $X_{\text{C}} \approx 3 \times 10^{-3}$, $X_{\text{N}} \approx 8 \times 10^{-3}$, and $X_{\text{O}} \approx 10^{-4}$, which is more consistent with an SAGB than an RSG atmosphere^{5,6}.

Since the core composition and explosion nucleosynthesis are different from Fe CCSNe (but see Methods for some caveats on the low-mass end), ECSNe are expected to show distinct nebular spectral features: stronger Ni than Fe lines due to a more stable ^{58}Ni yield than radioactive ^{56}Ni (a

parent nuclide of ^{56}Fe) from the innermost neutron-rich ejecta (electron fraction $Y_e \lesssim 0.49$)^{10, 11}; weak O, Mg, and Fe lines owing to the thin ($\sim 0.01 M_\odot$) O+C shell which is further burned to Fe-group elements^{7, 8}; and weak C lines because of the efficient dredge-up/out reducing most of the He-rich layer before the explosion^{4, 5, 6} (N lines are hard to be constrained in Type II-P SNe, as [N II] $\lambda\lambda 6548, 6583$ are hidden by strong $H\alpha$)²⁴. For low-mass progenitors ($\lesssim 12 M_\odot$), a low line ratio of [O I]/[Ca II] is expected due to the low O-core mass^{25, 26, 24}.

True nebular spectral models of ECSNe are difficult to produce, but they can be approximated by removing the He core from an Fe CCSN simulation. Here we use such a model¹¹, which we call the “approximate ECSN” model. Comparison of the nebular spectra of SN 2018zd with the $9 M_\odot$ models¹¹ favours the approximate ECSN model over the Fe CCSN model, especially through the weak C, O, Mg, and Fe lines (Fig. 4). In addition, the low line ratio of [O I] $\lambda\lambda 6300, 6364$ /[Ca II] $\lambda\lambda 7291, 7323 < 1$ observed in SN 2018zd indicates a low-mass progenitor.

Although quantitative analysis to derive the masses of Ni and Fe requires detailed radiative transfer simulations, we can obtain a rough estimate of the line ratio expected from ECSNe. For normal Fe CCSNe where Ni and Fe are dominantly produced in the same layer, [Fe II] overwhelms [Ni II] in the emission from the innermost region²⁵. In ECSN models¹⁰, however, there is a layer of Ni-rich (neutron-rich) material, emitting predominantly [Ni II], inside the outer mixture of Ni and Fe. In this situation where the Ni-rich and Fe-rich regions are physically separated, [Ni II]/[Fe II] roughly reflects the mass ratio of Ni and Fe in the entire ejecta^{26, 24} – 1.3–3.0 in the ECSN models¹⁰. The observed [Ni II] $\lambda 7378$ /[Fe II] $\lambda 7155$ ratio of 1.3–1.6 in SN 2018zd (Fig. 4) is indeed within

the expected range. In principle, clumping, fluorescence, and/or shock excitation could enhance [Ni II] λ 7378 such that [Ni II] λ 7378/[Fe II] λ 7155 overestimates the Ni/Fe mass ratio²⁷, but we leave a detailed theoretical study to future works.

SN 1054, whose remnant is the Crab Nebula, has been suggested as an ECSN candidate^{28, 29, 9, 18}. It shows He-, C-, and Ni-rich ejecta, but O- and Fe-poor abundances^{27, 30}, small ejecta mass ($4.6 \pm 1.8 M_{\odot}$)³¹, and low kinetic energy ($\sim 10^{49}$ erg)²⁹, although the observed relatively high neutron star kick velocity ($\sim 160 \text{ km s}^{-1}$) compared to those theoretically predicted for ECSNe ($< 10 \text{ km s}^{-1}$)³² is somewhat questionable. The slowly expanding filaments ($\sim 1,200 \text{ km s}^{-1}$) without a blast wave outside likely indicate the presence of CSM decelerating the SN ejecta^{31, 29}, and the historical light curve of SN 1054 may be similar to that of ECSNe^{29, 9, 18}. If both SNe 1054 and 2018zd are ECSNe, the differences may help us understand the diversity of the class, whilst the similarities may help us understand some of the properties of SN 1054 that remain unknown (see Methods and Extended Data Table 1 for other previously suggested ECSN candidates).

SN 2018zd fulfills the expected characteristics and is strong evidence for the existence of ECSNe and their progenitor SAGB stars, which puts constraints on many fields of physics and astrophysics (see Methods and Extended Data Fig. 9 for a rough ECSN rate calculation). Theoretically, the evolutionary path to SAGB stars is uncertain owing to the high sensitivity of nuclear burning on complex dredge-up/out and mass-loss mechanisms^{6, 5}, giving a variety of expected mass windows at different metallicities (e.g., $\Delta M_{\text{SAGB}} \sim 0.2\text{--}1.4 M_{\odot}$ at solar metallicity⁴). Their final fate may vary from core-collapse to thermonuclear ECSNe depending on the electron-capture rates

and oxygen flame speed in the degenerate core^{33,34}, resulting in different nucleosynthetic yields and galactic chemical evolution³⁵. The core-collapse ECSNe are expected to leave low mass, spin, and kick-velocity neutron stars³², forming a low-mass peak ($\sim 1.25 M_{\odot}$) in neutron star mass distribution³⁶ and low-eccentricity (~ 0.2) gravitational wave source population³⁷. Therefore, using SN 2018zd as an ECSN template, future statistical studies with large surveys will be able to further reveal the true nature, rate, and implications of ECSNe for stellar evolution, core-collapse physics, supernova remnants, cosmic nucleosynthesis, the neutron star mass distribution, and the gravitational wave source population.

1. Miyaji, S., Nomoto, K., Yokoi, K. & Sugimoto, D. Supernova triggered by electron captures. *Publications of the Astronomical Society of Japan* **32**, 303–329 (1980).
2. Nomoto, K. Evolution of 8-10 solar mass stars toward electron capture supernovae. I - Formation of electron-degenerate O + NE + MG cores. *Astrophys. J.* **277**, 791–805 (1984).
3. Nomoto, K. Evolution of 8–10 M_{sun} Stars toward Electron Capture Supernovae. II. Collapse of an O + NE + MG Core. *Astrophys. J.* **322**, 206 (1987).
4. Poelarends, A. J. T., Herwig, F., Langer, N. & Heger, A. The Supernova Channel of Super-AGB Stars. *Astrophys. J.* **675**, 614–625 (2008).
5. Jones, S. *et al.* Advanced Burning Stages and Fate of 8-10 M_{\odot} Stars. *Astrophys. J.* **772**, 150 (2013).

6. Doherty, C. L., Gil-Pons, P., Siess, L. & Lattanzio, J. C. Super-AGB Stars and their Role as Electron Capture Supernova Progenitors. *Publications of the Astronomical Society of Australia* **34**, e056 (2017).
7. Kitaura, F. S., Janka, H. T. & Hillebrandt, W. Explosions of O-Ne-Mg cores, the Crab supernova, and subluminous type II-P supernovae. *Astron. Astrophys.* **450**, 345–350 (2006).
8. Janka, H. T., Müller, B., Kitaura, F. S. & Buras, R. Dynamics of shock propagation and nucleosynthesis conditions in O-Ne-Mg core supernovae. *Astron. Astrophys.* **485**, 199–208 (2008).
9. Tominaga, N., Blinnikov, S. I. & Nomoto, K. Supernova Explosions of Super-asymptotic Giant Branch Stars: Multicolor Light Curves of Electron-capture Supernovae. *Astrophys. J. Letters* **771**, L12 (2013).
10. Wanajo, S., Nomoto, K., Janka, H. T., Kitaura, F. S. & Müller, B. Nucleosynthesis in Electron Capture Supernovae of Asymptotic Giant Branch Stars. *Astrophys. J.* **695**, 208–220 (2009).
11. Jerkstrand, A. *et al.* Emission line models for the lowest mass core-collapse supernovae - I. Case study of a $9 M_{\odot}$ one-dimensional neutrino-driven explosion. *Mon. Not. R. Astron. Soc.* **475**, 277–305 (2018).
12. Itagaki, K. Transient Discovery Report for 2018-03-02. *Transient Name Server Discovery Report* **2018-285**, 1 (2018).
13. de Vaucouleurs, G. *et al.* Book-Review - Third Reference Catalogue of Bright Galaxies. *Sky & Telescope* **82**, 621 (1991).

14. Arcavi, I. *et al.* Global SN Project Transient Classification Report for 2018-03-06. *Transient Name Server Classification Report* **2018-2082**, 1 (2018).
15. Adamo, A. *et al.* Revealing a ring-like cluster complex in a tidal tail of the starburst galaxy NGC 2146. *Mon. Not. R. Astron. Soc.* **426**, 1185–1194 (2012).
16. Valenti, S. *et al.* The diversity of Type II supernova versus the similarity in their progenitors. *Mon. Not. R. Astron. Soc.* **459**, 3939–3962 (2016).
17. Spiro, S. *et al.* Low luminosity Type II supernovae - II. Pointing towards moderate mass precursors. *Mon. Not. R. Astron. Soc.* **439**, 2873–2892 (2014).
18. Moriya, T. J. *et al.* Electron-capture supernovae exploding within their progenitor wind. *Astron. Astrophys.* **569**, A57 (2014).
19. Ofek, E. O. *et al.* Supernova PTF 09UJ: A Possible Shock Breakout from a Dense Circumstellar Wind. *Astrophys. J.* **724**, 1396–1401 (2010).
20. Moriya, T. J., Förster, F., Yoon, S.-C., Gräfener, G. & Blinnikov, S. I. Type IIP supernova light curves affected by the acceleration of red supergiant winds. *Mon. Not. R. Astron. Soc.* **476**, 2840–2851 (2018).
21. Yaron, O. *et al.* Confined dense circumstellar material surrounding a regular type II supernova. *Nature Physics* **13**, 510–517 (2017).
22. Boian, I. & Groh, J. H. Diversity of supernovae and impostors shortly after explosion. *Astron. Astrophys.* **621**, A109 (2019).

23. Boian, I. & Groh, J. H. Progenitors of early-time interacting supernovae. *arXiv e-prints* arXiv:2001.07651 (2020).
24. Fang, Q. & Maeda, K. The Origin of the Ha-like Structure in Nebular Spectra of Type IIb Supernovae. *Astrophys. J.* **864**, 47 (2018).
25. Jerkstrand, A. *et al.* The progenitor mass of the Type IIP supernova SN 2004et from late-time spectral modeling. *Astron. Astrophys.* **546**, A28 (2012).
26. Maeda, K. *et al.* SN 2006aj Associated with XRF 060218 at Late Phases: Nucleosynthesis Signature of a Neutron Star-driven Explosion. *Astrophys. J. Letters* **658**, L5–L8 (2007).
27. Hudgins, D., Herter, T. & Joyce, R. J. The Ni/Fe Ratio in the Crab Nebula. *Astrophys. J. Letters* **354**, L57 (1990).
28. Nomoto, K. *et al.* The Crab Nebula’s progenitor. *Nature* **299**, 803–805 (1982).
29. Smith, N. The Crab nebula and the class of Type IIn-P supernovae caused by sub-energetic electron-capture explosions. *Mon. Not. R. Astron. Soc.* **434**, 102–113 (2013).
30. Satterfield, T. J., Katz, A. M., Sibley, A. R., MacAlpine, G. M. & Uomoto, A. Element Distributions in the Crab Nebula. *Astron. J.* **144**, 27 (2012).
31. Fesen, R. A., Shull, J. M. & Hurford, A. P. An Optical Study of the Circumstellar Environment Around the Crab Nebula. *Astron. J.* **113**, 354–363 (1997).
32. Gessner, A. & Janka, H.-T. Hydrodynamical Neutron-star Kicks in Electron-capture Supernovae and Implications for the CRAB Supernova. *Astrophys. J.* **865**, 61 (2018).

33. Zha, S., Leung, S.-C., Suzuki, T. & Nomoto, K. Evolution of ONeMg Core in Super-AGB Stars toward Electron-capture Supernovae: Effects of Updated Electron-capture Rate. *Astrophys. J.* **886**, 22 (2019).
34. Leung, S.-C., Nomoto, K. & Suzuki, T. Electron-capture Supernovae of Super-AGB Stars: Sensitivity on Input Physics. *Astrophys. J.* **889**, 34 (2020).
35. Jones, S., Côté, B., Röpke, F. K. & Wanajo, S. A New Model for Electron-capture Supernovae in Galactic Chemical Evolution. *Astrophys. J.* **882**, 170 (2019).
36. Schwab, J., Podsiadlowski, P. & Rappaport, S. Further Evidence for the Bimodal Distribution of Neutron-star Masses. *Astrophys. J.* **719**, 722–727 (2010).
37. Giacobbo, N. & Mapelli, M. The impact of electron-capture supernovae on merging double neutron stars. *Mon. Not. R. Astron. Soc.* **482**, 2234–2243 (2019).
38. Hosseinzadeh, G. *et al.* Short-lived Circumstellar Interaction in the Low-luminosity Type IIP SN 2016bkv. *Astrophys. J.* **861**, 63 (2018).
39. Gal-Yam, A. *et al.* A Wolf-Rayet-like progenitor of SN 2013cu from spectral observations of a stellar wind. *Nature* **509**, 471–474 (2014).

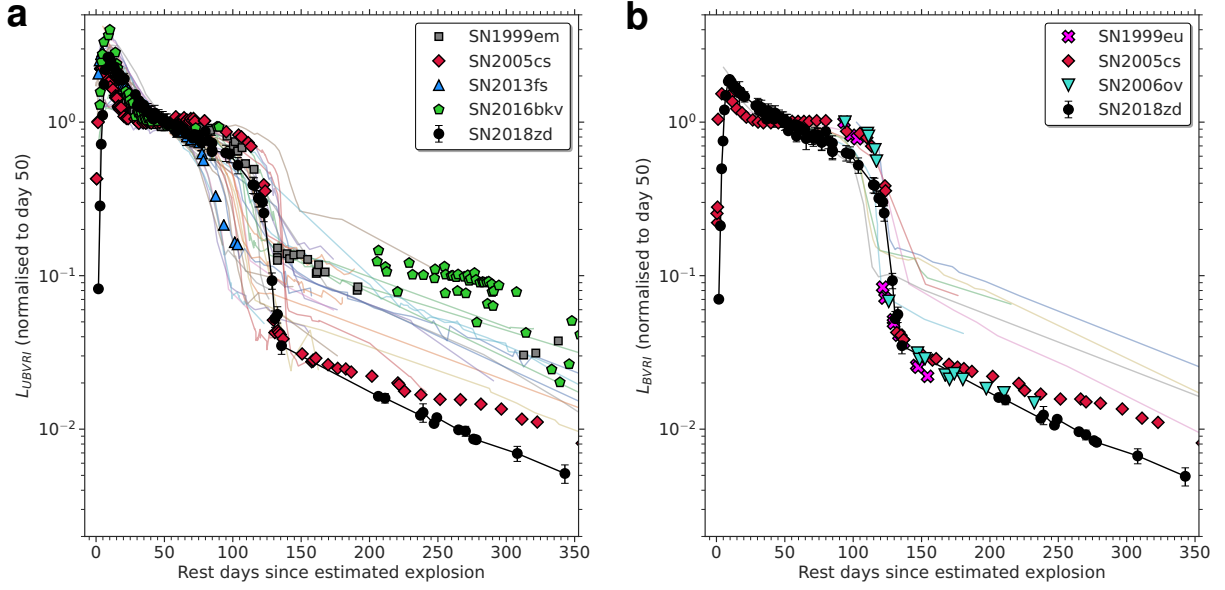


Figure 1 Normalised pseudobolometric light curves. (a) Comparison of the normalised pseudobolometric ($UBVR$; see Methods) light curve of SN 2018zd with a well-observed Type II SN sample¹⁶ (transparent lines), including archetypal SN 1999em, low-luminosity SN 2005cs, and early-flash SN 2013fs, along with low-luminosity and early-flash SN 2016bkv³⁸. (b) Comparison of the normalised pseudobolometric ($BVRI$) light curve of SN 2018zd with a low-luminosity Type II-P SN sample¹⁷, including SNe 1999eu and 2006ov with the largest plateau drops ever to our knowledge. Error bars denote 1σ uncertainties. Because of the distance uncertainty of SN 2018zd, we normalise each light curve to day 50 and make the comparisons distance independent. SN 2018zd shows the largest plateau drop that is comparable to SNe 1999eu and 2006ov, indicating an intrinsically low ^{56}Ni production.

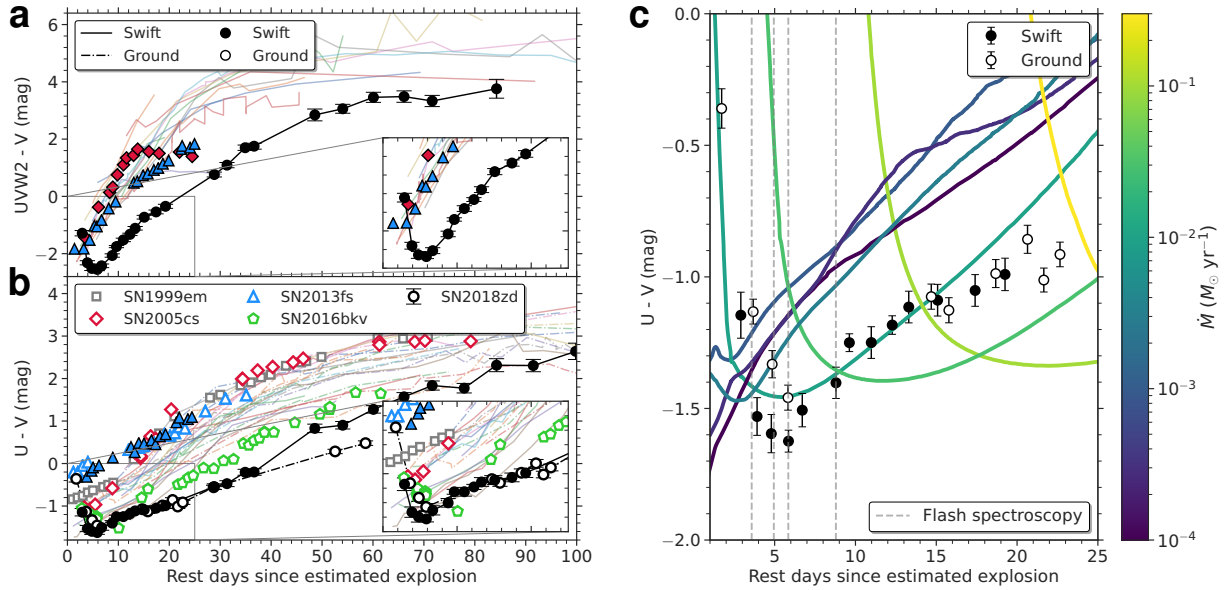


Figure 2 UV colour light curves. (a, b) Comparison of the UV colours of SN 2018zd with the sample as in Fig. 1a. Error bars denote 1σ uncertainties. Note the pronounced sharp blueward colour evolution of SN 2018zd over the first ~ 5 d, shown in the insets, suggesting a possible delayed shock-breakout through dense CSM. **(c)** Comparison of the $U-V$ colour of SN 2018zd with our MESA+STELLA CSM models (see Methods and Extended Data Fig. 6) assuming a typical constant wind velocity of 20 km s^{-1} (Fig. 3), colour-coded by the mass-loss rate. To reproduce the observed early blueward evolution, $\dot{M} \approx 0.01 M_{\odot} \text{ yr}^{-1}$ for the last ~ 10 yr before the explosion is required. The observed flash-spectroscopy epochs (Fig. 3) are marked by the vertical dashed lines and are consistent with the blueward colour evolution.

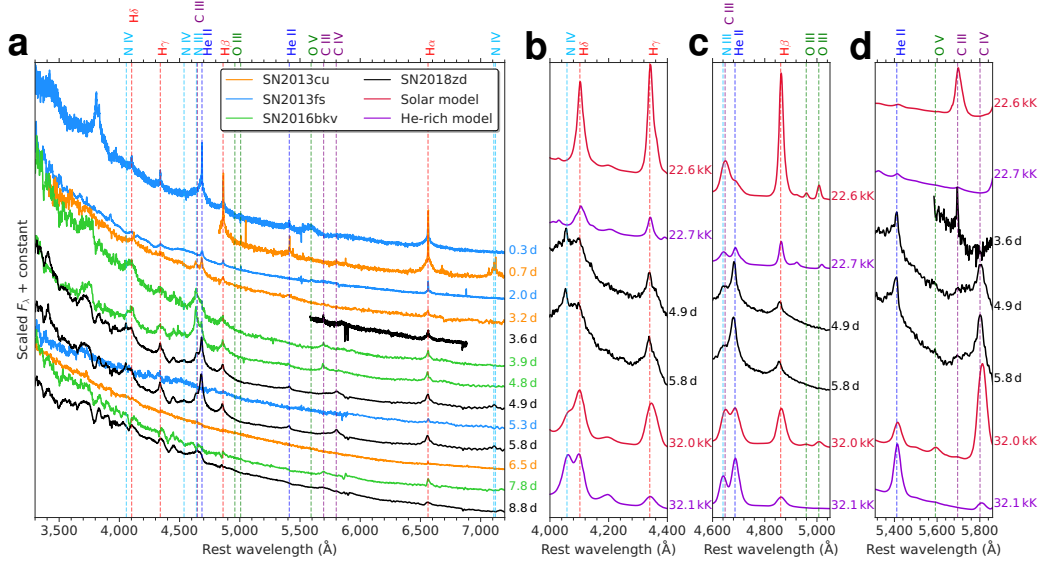


Figure 3 Flash spectral time series. (a) Comparison of the flash spectral time series of SN 2018zd with well-sampled Type II-P SNe 2013fs²¹ and 2016bkv³⁸, and Type IIb (mostly stripped H-rich envelope) SN 2013cu³⁹. SN 2018zd exhibits the persistent flash features ($\gtrsim 9$ d), whilst most of the flash features in the other SNe disappear within ~ 5 d after the explosion. (b, c, d) Comparison of SN 2018zd with the scaled and resampled flash spectral models of solar abundance ($X_{\text{H}} = 0.70$, $X_{\text{He}} = 0.28$, $X_{\text{C}} = 3.02 \times 10^{-3}$, $X_{\text{N}} = 1.18 \times 10^{-3}$, $X_{\text{O}} = 9.63 \times 10^{-3}$) and He-rich ($X_{\text{H}} = 0.18$, $X_{\text{He}} = 0.80$, $X_{\text{C}} = 5.58 \times 10^{-5}$, $X_{\text{N}} = 8.17 \times 10^{-3}$, $X_{\text{O}} = 1.312 \times 10^{-4}$) atmosphere with $\dot{M}_{\text{mod}} = 3 \times 10^{-3} M_{\odot} \text{yr}^{-1}$ and $v_{\text{mod}} = 150 \text{ km s}^{-1}$ (the densest CSM with the finest temperature grid spacing)²². The temperatures are constrained to be within $\sim 20,000$ K (at 3.6 d) to 30,000 K (at 4.9–5.8 d) from the MESA+STELLA UV-colour models (Fig. 2). The observed features are expected

to be narrower and stronger if resolved, as $\rho_{\text{obs}}/\rho_{\text{mod}} = (\dot{M}_{\text{obs}}/v_{\text{obs}})/(\dot{M}_{\text{mod}}/v_{\text{mod}}) = 25$ with $\dot{M}_{\text{obs}} = 0.01 M_{\odot} \text{ yr}^{-1}$ from the UV colours and assuming $v_{\text{obs}} = 20 \text{ km s}^{-1}$ (the wind P-Cygni components of SN 2018zd are not resolved, only giving an upper-limit $v_{\text{obs}} < 76.3 \text{ km s}^{-1}$ from the highest spectral resolution of C III $\lambda 5696$ at 3.6 d). Based on the model comparisons, the line ratios of N IV/H $\delta > 1$ (b) and He II/H $\beta > 1$ (c), the transition from C III to C IV (d), and the lack of O III and O V lines (c, d) observed in SN 2018zd suggest He-, C-, and N-rich, but O-poor CSM composition.

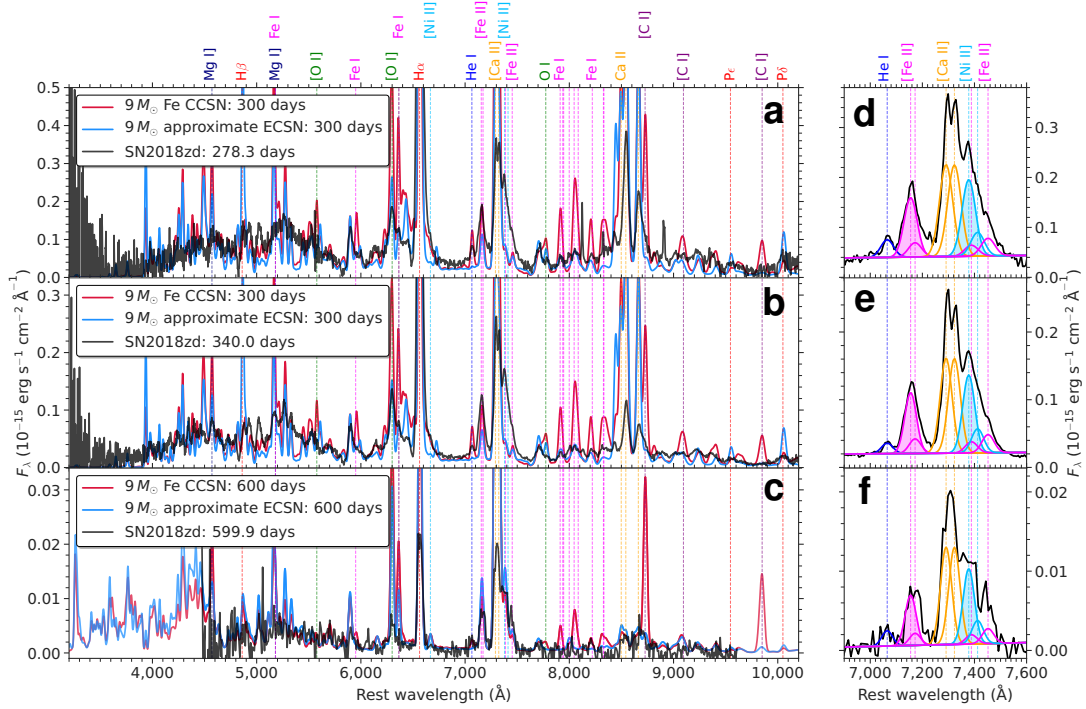


Figure 4 Nebular spectral time series. (a, b, c) Comparison of the nebular spectral time series of SN 2018zd with the scaled (by ^{56}Ni mass and phase) and resampled $9 M_{\odot}$ Fe CCSN and “approximate ECSN” (excluding the He-core composition from the Fe CCSN) models¹¹. The large number of narrow lines at $\lesssim 5500 \text{ \AA}$ and strong Ca lines in the models are known issues. The weak [Ni II] lines in the models are from the primordial Ni (solar abundance), as Ni nucleosynthesis is not taken into account. In ascending order of wavelength, note the weak Mg I] $\lambda 4571$, Mg I] $\lambda 5180$ + Fe I $\lambda 5180$, [O I] $\lambda 5577$, Fe I $\lambda 5950$, [O I] $\lambda\lambda 6300, 6364$ + Fe I $\lambda 6364$, O I $\lambda 7774$, Fe I cluster $7900\text{--}8500 \text{ \AA}$, [C I] $\lambda 8727$, [C I] $\lambda 9100$, and [C I] $\lambda 9850$, as well as the low line ratio of [O I] $\lambda\lambda 6300, 6364$ /[Ca II]

$\lambda\lambda 7291, 7323 < 1$ observed in SN 2018zd. He I $\lambda 7065$ is weaker in the approximate ECSN model than in the observed spectra; the emission from the dredged-up/out elements (e.g., He and N) in the H-rich envelope may be underestimated by the model. **(d, e, f)** Simultaneous Gaussian fits to He I $\lambda 7065$, [Fe II] $\lambda 7155$, [Fe II] $\lambda 7172$, [Ca II] $\lambda 7291$, [Ca II] $\lambda 7323$, [Ni II] $\lambda 7378$, [Fe II] $\lambda 7388$, [Ni II] $\lambda 7412$, and [Fe II] $\lambda 7452$ (see Methods). Note the stronger [Ni II] $\lambda 7378$ (the blue shaded region) than [Fe II] $\lambda 7155$ (the pink shaded region), yielding $[\text{Ni II}]/[\text{Fe II}] = 1.3\text{--}1.6$. The weak C, O, Mg, and Fe lines combined with the strong Ni lines observed in SN 2018zd are consistent with the ECSN chemical composition and nucleosynthesis.

Methods

Follow-up imaging. Follow-up imaging was obtained with the Las Cumbres Observatory network of 0.4 m, 1 m, and 2 m telescopes⁴⁰ through the Global Supernova Project, the Neil Gehrels *Swift* Observatory Ultraviolet/Optical Telescope (UVOT), the Noguchi Astronomical Observatory (Chiba, Japan) 0.26 m telescope, and the Itagaki Astronomical Observatory (Okayama and Tochigi, Japan) 0.35 m and 0.5 m telescopes. For the Las Cumbres photometry, point-spread-function (PSF) fitting was performed using `lcogtsnpipe`¹⁶, a PyRAF-based photometric reduction pipeline. *UBV*- and *gri*-band data were calibrated to Vega⁴¹ and AB⁴² magnitudes, respectively, using standard fields observed on the same night by the same telescope as the SN. The *Swift* UVOT photometry was done using the pipeline for the *Swift* Optical Ultraviolet Supernova Archive (SOUSA)⁴³, including the updated sensitivity corrections and zeropoints⁴⁴ and the subtraction of the underlying host-galaxy count rates using images from October/November 2019. The unfiltered optical Itagaki (KAF-1001E CCD) and Noguchi (ML0261E CCD) photometry was extracted using `Astrometrica`⁴⁵ and calibrated to the Fourth US Naval Observatory CCD Astrograph Catalog (UCAC4)⁴⁶. All photometry will be available for download via the Weizmann Interactive Supernova Data Repository (WiSeREP)⁴⁷ and the Open Supernova Catalog⁴⁸. We correct all photometry for the Milky Way (MW) and host-galaxy extinction (see Section Extinction and Extended Data Fig. 3).

We estimate an explosion epoch by fitting a quadratic function $F_1(t - t_0)^2$ to the unfiltered Itagaki and first three Noguchi points with similar CCD spectral responses ($\lambda_{\text{eff}} = 6500\text{--}6700 \text{ \AA}$), where the effect of CSM interaction is less prominent than in the UV bands (Extended Data Fig. 3). This

yields an explosion epoch $t_0 = \text{MJD } 58178.4 \pm 0.1$, where the uncertainty is estimated from the difference between the explosion epoch and the first Itagaki detection. Even if we use the most conservative explosion epoch of the last nondetection on MJD 58175.5, the difference is only 2.9 rest-frame days, not affecting the main results of this paper.

We fit a blackbody spectral energy distribution (SED) to every epoch of the Las Cumbres and *Swift* photometry containing at least three filters (excluding the r band owing to strong $\text{H}\alpha$ contamination) obtained within 0.3 d of each other to estimate the blackbody temperature and radius at the assumed luminosity distance (note that the observed SED peaks are bluer than the Swift wavelength coverage between 3–10 d after the explosion, potentially underestimating the blackbody temperatures¹⁶). Then we integrate the fitted blackbody SED to obtain bolometric (and pseudobolometric) luminosity at each epoch. Since we only have the unfiltered Noguchi photometry during the plateau drop owing to the Sun constraint, we estimate a bolometric (and pseudobolometric) correction by finding the offset of the Noguchi photometry to the Las Cumbres and *Swift* integrated bolometric (and pseudobolometric) luminosity during the plateau phase (50–80 d) where most of the SED ($\sim 80\%$) is in the spectral response range of the unfiltered CCD. Then we apply the bolometric (and pseudobolometric) correction to the Noguchi photometry and include it in the bolometric (and pseudobolometric) light curve during the plateau drop (Fig. 1). This procedure is also justified by the good agreement with the tail bolometric (and pseudobolometric) luminosity obtained from the Las Cumbres multiband photometry after the Sun constraint.

Follow-up spectroscopy. Follow-up spectroscopy was obtained with the FLOYDS spectrograph mounted on the Las Cumbres Observatory 2 m Faulkes Telescope North (FTN)⁴⁰ through the

Global Supernova Project, the Boller & Chivens (B&C) spectrograph mounted on the 2.3 m Bok telescope, the Blue Channel (BC) spectrograph mounted on the 6.5 m MMT, and the Low Resolution Imaging Spectrometer (LRIS)^{49, 50, 51} and the DEep Imaging Multi-Object Spectrograph (DEIMOS)⁵² mounted on the 10 m Keck-I and Keck-II telescopes, respectively. For the FLOYDS observations, a 2'' slit was placed on the target at the parallactic angle⁵³ (to minimise the effects of atmospheric dispersion). One-dimensional spectra were extracted, reduced, and calibrated following standard procedures using the FLOYDS pipeline⁵⁴. The Bok low-resolution optical spectra were taken with the 300 lines mm⁻¹ grating using a 1.5'' slit width, and the MMT moderate-resolution spectra were obtained using a 1.0'' slit width. The spectra were reduced using standard techniques in IRAF, including bias subtraction, flat-fielding, and sky subtraction. Flux calibration was done with spectrophotometric standard star observations taken on the same night at similar airmass. The Keck LRIS spectra were reduced using the `Lpipe` pipeline⁵⁵ with the default parameters and standard spectroscopic reduction techniques. The Keck DEIMOS spectrum was reduced with a custom-made Python pipeline that performs flat-field correction, sky subtraction, optimal extraction⁵⁶, and flux calibration using a standard star observed on the same night as the SN. All spectra will be available for download via WISeREP and the Open Supernova Catalog. We correct all spectra for the MW and host-galaxy extinction and calibrate the flux using the photometry (Extended Data Fig. 4).

We measure expansion velocities of H α , H β , and Fe II λ 5169 from the absorption minimum by fitting a P-Cygni profile to each line. Then we translate the difference between the observed minimum and the rest wavelength of the line to an expansion velocity using the relativistic Doppler

formula (Extended Data Fig. 5). We estimate the velocity uncertainties by randomly varying the background region by $\pm 5 \text{ \AA}$.

We simultaneously fit Gaussian functions to He I $\lambda 7065$, [Fe II] $\lambda 7155$, [Fe II] $\lambda 7172$, [Ca II] $\lambda 7291$, [Ca II] $\lambda 7323$, [Ni II] $\lambda 7378$, [Fe II] $\lambda 7388$, [Ni II] $\lambda 7412$, and [Fe II] $\lambda 7452$ in the nebular spectra assuming a single full width at half-maximum (FWHM) velocity for all lines and the theoretically expected line ratios for the [Ca II], [Fe II], and [Ni II] lines⁵⁷ (Fig. 4). The resultant [Ni II] $\lambda 7378$ /[Fe II] $\lambda 7155$ ratios and FWHM velocities are 1.3–1.6 and 2,500–2,100 km s^{-1} , respectively, from 278–600 d after the explosion.

Follow-up spectropolarimetry. Follow-up spectropolarimetric observations of SN 2018zd were obtained using the CCD Imaging/Spectropolarimeter (SPOL⁵⁸) on the 6.5 m MMT telescope using a 2.8'' slit on 2018 April 23 (53 d after the explosion). We used a 964 lines mm^{-1} grating with a typical wavelength coverage of 4050–7200 \AA and a resolution of $\sim 29 \text{ \AA}$. We used a rotatable semi-achromatic half-wave plate to modulate incident polarization and a Wollaston prism in the collimated beam to separate the orthogonally polarized spectra onto a thinned, anti-reflection-coated 800×1200 pixel SiTe CCD. The efficiency of the wave plate as a function of wavelength was measured and corrected for by inserting a fully-polarizing Nicol prism into the beam above the slit. A series of four separate exposures that sample 16 orientations of the wave plate yield two independent, background-subtracted measures of each of the normalised linear Stokes parameters, Q and U . Two such sequences were acquired and combined to increase the signal-to-noise ratio.

Our spectropolarimetric analysis is performed primarily using the linear Stokes parameters, $q = Q/I$ and $u = U/I$, which are rotated 45° with respect to each other, allowing us to decompose the polarization signal into orthogonal components in position-angle space. We use the debiased polarization level, $p_{\text{db}} = \sqrt{|(q^2 + u^2) - \frac{1}{2}(\sigma_q^2 + \sigma_u^2)|}$, in favour of the standard polarization level, $p = \sqrt{q^2 + u^2}$, because the standard polarization level is a positive-definite quantity that measures the distance from the origin in a q vs. u plane. When the signal-to-noise ratio is low, this positive-definite quantity can be misleading, whereas the debiased polarization value accounts for large uncertainty in measurements of q and u .

SN 2018zd exhibits a mean polarization of 0.9% across the continuum at 5100–5700 Å and 0.8% across the continuum at 6000–6300 Å. However, the polarization does not vary much across the entire spectrum, even across absorption and emission-line features. Typically, a polarized continuum would become depolarized across emission-line features due to dilution with unpolarized light from the emission line. Since SN 2018zd does not exhibit any such changes across any of its emission-line features, we suggest that the majority of the polarization signal arises in the interstellar medium rather than in the SN itself. The Serkowski relation⁵⁹ suggests that $p_{\text{max}} < 9 E(B - V)$. If all 0.9% of the continuum peak polarization in SN 2018zd were due to the interstellar medium, then we could estimate the extinction to be $E(B - V) > p_{\text{max}}/9 = 0.1$ mag and a reddening of at least $A_V = 3.1 E(B - V) = 0.31$ mag.

Extinction. We obtained the MW extinction⁶⁰ of $A_{V,\text{MW}} = 0.258$ mag via the NASA/IPAC Infrared Science Archive⁶¹. We measure the total Na I D EW of each host and MW component using the MMT BC spectra (moderate resolution of 1.45 Å) taken between 3.6–53.4 d after the explo-

sion. Since the ratio of the total Na I D EW of the host to MW varies between 1.07 and 1.25, we estimate $A_{V,\text{host}} \gtrsim A_{V,\text{MW}}$. As a cross-check, we transform the *gri* magnitudes of SN 2018zd to *VRI* magnitudes⁶² and compare the *V-I* colour to that of well-observed, low-extinction Type II-P SNe 1999em⁶³, 1999gi⁶⁴, 2012aw⁶⁵, and 2017eaw⁶⁶ by assuming $A_{V,\text{host}} = A_{V,\text{MW}}$ for SN 2018zd. Since the *V-I* colour of SN 2018zd during the photospheric phase is consistent with the other SNe, we adopt a host extinction of $A_{V,\text{host}} = A_{V,\text{MW}}$ and assume a reddening⁶⁷ law with $R_V = 3.1$, consistent with the lower limit obtained from the spectropolarimetry. Increasing (or decreasing) the host extinction by more than 0.10 mag makes the *V-I* colour inconsistent with that of the other Type II-P SNe. Thus, we adopt a host extinction uncertainty of ± 0.10 mag.

Luminosity distance. We apply the expanding photosphere method (EPM)^{64, 68} and the standard candle method (SCM)⁶⁹ using the measured Fe II $\lambda 5169$ velocities and transforming the *gri* to *VRI* magnitudes⁶², which yields 6.5 ± 0.7 and 9.6 ± 1.0 Mpc, respectively. The EPM is best used at early times ($\lesssim 30$ d) when SN emission can be approximated as a diluted blackbody in free expansion⁶⁸. However, the early emission from SN 2018zd is dominated by CSM interaction (Fig. 2 and Extended Data Fig. 5), making the EPM unreliable. On the other hand, the SCM is based on the luminosity–velocity correlation^{70, 71, 72} at day 50 when the CSM interaction is negligible, which is well reproduced by our MESA+STELLA models (see Section MESA+STELLA progenitor and light-curve modeling and Extended Data Fig. 6). Thus, we favour the SCM over the EPM.

It has been suggested that NGC 2146 may be further than the SCM estimate. There is a claim of a preliminary tip of the red giant branch (TRGB) distance obtained from archival *HST* WFC3/IR data (program GO-12206, PI: M. Westmoquette) that places the galaxy out at ~ 18 Mpc¹⁵. We

have independently reduced and analysed this same data and find that the single orbit of observations available (split between F110W & F160W) do not reach the necessary depths to make this conclusion. Even at the closer 10 Mpc distance, the archival data would not allow us to obtain a TRGB measurement due to the short exposure times and intense levels of crowding. We also find that there are no archival *HST* optical data of sufficient depths to obtain a TRGB measurement.

Future SN-independent distance measurements⁷³ (e.g., Cepheids and TRGB with *HST*) will be necessary to verify the SCM estimate. We discuss the implications if the luminosity distance were larger than the SCM estimate in Section Alternative scenarios.

Host galaxy. NGC 2146 is an edge-on spiral galaxy with several tidal streams that were likely ejected during a galaxy merger event ~ 800 Myr ago⁷⁴ (Extended Data Fig. 1). The presence of a starburst-driven superwind from the bulge is revealed across the electromagnetic spectrum from γ -rays to infrared^{75, 76, 74, 77}, indicating an ongoing high star formation rate⁷⁸ ($\text{SFR} \approx 10 M_{\odot} \text{ yr}^{-1}$). Based on radio observations of the bulge⁷⁹, there are many more dense H II regions (each containing up to 1,000 type O6 stars) than supernova remnants, suggesting a relatively young phase of the starburst. The bulge has a high dust content and roughly solar metallicity ($12 + \log_{10}[\text{O}/\text{H}] = 8.68 \pm 0.10$)^{78, 80}. Since SN 2018zd is at a relatively large separation from the nucleus of $1'83$ north-west ($36''.1$ north, $103''.7$ west; Extended Data Fig. 1), and the galactic radius parameter $R_{25} = 1'.78$ (via NASA/IPAC Extragalactic Database⁸¹), if we reasonably assume that there is an abundance gradient for the galaxy, the metallicity at the SN site is likely subsolar; this merits future investigations once the SN fades.

***HST* and *Spitzer* progenitor detection and upper limits.** We were able to locate astrometrically the site of SN 2018zd in existing pre-explosion *HST* archival images, specifically data obtained in bands F814W and F658N with the ACS/WFC instrument on 2004 April 10 (program GO-9788, PI L. Ho, with total exposure times of 120 s and 700 s, respectively; the F814W image consists of a single exposure), as well as in F225W with WFC3/UVIS on 2013 March 7 (program GO-13007, PI L. Armus; total exposure time of 1500 s). Other *HST* data have been obtained of the host galaxy in other bands with other instruments, but these do not contain the SN site. We initially matched the F814W image with a Las Cumbres *V*-band image of fair quality (seeing 1''8) obtained at the McDonald Observatory facility on 2018 March 5.11, using 8 stars in common between the ground-based and *HST* data, with a root-mean-square (RMS) uncertainty in the astrometric solution of 1.99 ACS/WFC pixels. On visual inspection we found the site to be quite sparse, but we were able to identify a potential candidate progenitor in the ACS image within the 1σ positional uncertainty.

We confirmed the candidate more precisely by obtaining images of the SN itself on 2019 May 19 in F555W and F814W with WFC3/UVIS, as part of program GO-15151 (PI S. Van Dyk). We were able to astrometrically register the 2019 F814W image mosaic to the 2004 one using 23 stars in common, with an RMS uncertainty of 0.14 ACS/WFC pixel. Furthermore, in a similar fashion we were able to match precisely the SN image with the F658N and F225W images as well; however, the progenitor candidate was not detected in either of those bands. We show the pre- and post-explosion images in Extended Data Figure 1.

We extracted photometry from all of the *HST* images using the package Dolphot⁸². We applied Dolphot to the individual FLC frames. We found that Dolphot detected and measured a source

at the position of the progenitor candidate with $m_{F814W} = 25.05 \pm 0.15$ mag. Unfortunately, as noted above, the F814W pre-explosion observation consisted of only a single exposure, so it was not possible for the standard STScI pipeline to reject cosmic-ray hits in the usual way, whilst constructing an image mosaic from the single frame, as would normally be the case for two or more dithered exposures. Additionally, we note that the flux measurement with Dolphot may also be affected by the presence of cosmic-ray hits in the image at or around the progenitor site. Nevertheless, the values of both the Dolphot output parameters “object type” (1) and “sharpness” (-0.013) appear to point to the source being stellar-like. To determine whether the peak pixel seen at the candidate location is indeed merely a cosmic-ray hit or is the actual peak of a stellar PSF, we employ a deep learning model (Xu et. al., in preparation) based on the results from DeepCR⁸³. We find that no pixels in the vicinity of the candidate progenitor have a model score higher than 5.1×10^{-5} . If we use this score as a threshold, the model has a completeness of 99.93% based on the test data taken with the same instrument. We therefore conclude that progenitor candidate is a real PSF with $> 3\sigma$ confidence. If the object was not actually detected, we find that the upper limit at 3σ to detection in F814W is > 26.3 mag. Inserting and recovering an artificial star of varying brightness at the exact SN position with Dolphot in both F225W and F658N led to estimates of the upper limits to detection (at 3σ) of > 23.6 and > 24.1 mag, respectively. We also note that we measured a brightness of the SN itself in the 2019 *HST* observations of $m_{F555W} = 21.53 \pm 0.01$ and $m_{F814W} = 20.33 \pm 0.01$ mag.

The SN site also can be found in pre-explosion *Spitzer* data both from the cryogenic and so-called “Warm” (post-cryogenic) missions, from 3.6 to 24 μm . The data are from observations with

the Infrared Array Camera (IRAC⁸⁴) in channels 1 (3.6 μm) and 2 (4.5 μm ; the SN site sits in a gap of spatial coverage in channels 3 and 4 at 5.8 and 8.0 μm , respectively) on 2004 March 8 (program 59, PI G. Rieke) and on 2007 October 16 (program 40410, PI G. Rieke) in channels 2 and 4; from observations with the Multiband Imaging Photometer for Spitzer (MIPS⁸⁵) at 24 μm on 2004 March 16 (program 59, PI G. Rieke; the sensitivity and resolution of the data at 70 and 160 μm are not sufficient to hope to detect the progenitor and were not considered further); and from observations with IRAC in channels 1 and 2 on 2011 November 15 (program 80089, PI D. Sanders). We show the 2011 November 15 IRAC observation in ch1 in Extended Data Figure 1.

Observations with IRAC of the SN itself were obtained on 2019 January 24 (program 14098, PI O. Fox); however, we did not analyse these data, other than to extract an absolute position for the SN of $\alpha = 6^{\text{hr}}18^{\text{m}}03.43^{\text{s}}$, $\delta = +78^{\circ}22'01''.4$ (J2000; $\pm 0''.3$ in each coordinate). Using MOPEX⁸⁶ we constructed mosaics from all of the useful pre-SN imaging data, and with APEX within MOPEX⁸⁷ we inserted into the images an artificial star of varying brightness at this absolute position. From this we estimated upper limits to detection of the progenitor (at 3σ) of > 19.0 and > 18.1 mag in ch1 and ch2 (respectively) from the 2004 March 8 data; > 18.1 and > 14.5 mag in ch2 and ch4 (respectively) from 2007 October 16; and > 19.0 and > 18.4 mag in ch1 and ch2 (respectively) from 2011 November 15 (we have assumed the zeropoints from the IRAC Instrument Handbook⁸⁸). We also estimated > 10.2 mag at 24 μm from the 2004 March 16 observation (we have assumed the zeropoint from the MIPS Instrument Handbook⁸⁹).

We show the resulting SED, or limits thereon, for the SN 2018zd progenitor in Extended Data Figure 2. The distance (9.6 ± 1.0 Mpc) and extinction ($A_V = 0.52 \pm 0.10$ mag) to the SN dis-

cussed in Sections Luminosity distance and Extinction were adopted, assuming that the latter also applied to the progenitor as well. We have further assumed a reddening⁶⁷ law with $R_V = 3.1$ and extend it into the mid-infrared⁹⁰. For comparison we also show single-star models from BPASS v2.2⁹¹, specifically those for SAGB stars (i.e., those in the initial mass range $M_{\text{init}} = 6\text{--}8 M_{\odot}$ with bolometric luminosities $L \approx 10^5 L_{\odot}$ in the last model timestep) and RSG stars with $M_{\text{init}} = 8 M_{\odot}$ and $M_{\text{init}} = 15 M_{\odot}$. Here we considered the models with metallicities $Z = 0.020$ (solar) and $Z = 0.010$ (subsolar; as discussed in Section Host galaxy, the SN site metallicity is likely subsolar). We have extrapolated the SEDs of the BPASS models into the mid-infrared via MARCS⁹² model stellar atmospheres of similar temperatures as the last BPASS model timesteps, deriving synthetic photometry from those atmosphere models using the bandpass throughputs provided in the IRAC and MIPS Instrument Handbooks. We have further included for comparison the observed SED for the candidate SAGB star MSX SMC 055 (IRAS 00483–7347)⁹³, assuming Galactic foreground extinction and adjusted to a Small Magellanic Cloud distance modulus of $\mu = 18.90$ mag (Extragalactic Distance Database⁹⁴), as well as the SED for the progenitor of the low-luminosity Type II-P SN 2005cs^{95, 96}, assuming the total reddening from the two studies of that progenitor and adjusted to a recent accurate distance for M51⁹⁷. Note that the SEDs for the BPASS RSG models with $M_{\text{init}} = 15 M_{\odot}$ are likely not realistic, since they are merely bare photospheres, whereas we would expect such a star to possess a dusty CSM, as was the case for the progenitor of SN 2017eaw⁶⁶. The same could also potentially be said for the SAGB models, given the dusty nature of MSX SMC 055. Again, these BPASS model SEDs are bare photospheres and do not include CSM, of which we have strong evidence (given here) for the presence in the case of the SN 2018zd

progenitor; this merits further development of the SED models including the effect of dusty CSM.

It is difficult to infer much about the nature of the SN 2018zd progenitor, based on a probable detection in one band and upper limits in the others. However, its inferred SED does appear to be less consistent with that of an $M_{\text{init}} \gtrsim 8 M_{\odot}$ RSG star, as well as the SN 2005cs progenitor, and more consistent with a potentially dusty SAGB star, such as MSX SMC 055. If there were circumstellar dust around the SN 2018zd progenitor, it was destroyed as the SN shock progressed through.

We should revisit this site either with *HST* or the *James Webb Space Telescope* in a bandpass similar to F814W, when the SN has sufficiently faded, to confirm that the candidate object was indeed the progenitor. Again, we cannot entirely rule out that the source detected in the pre-SN image at the precise SN position is not related to a cosmic-ray hit, however, all of the indications are that this is a real detected star, which should have vanished when the SN site is observed at a sufficiently late time.

MESA+STELLA progenitor and light-curve modeling. Recent work^{72, 98, 99, 100} highlights the nonuniqueness of bolometric light-curve modeling for extracting explosion characteristics (ejecta mass M_{ej} , explosion energy E_{exp} , and progenitor radius R) from plateau features (in particular, luminosity at day 50, L_{50} , and plateau duration, t_p) without an independent prior on one of M_{ej} , E_{exp} , or R . Due to the presumed presence of a dense CSM and its potential influence on the early light curves and velocities, shock-cooling modeling and early expansion velocities cannot simply lift this degeneracy.

To allow light-curve analysis to be agnostic to the progenitor mass, three different explosion models were created with equally good by-eye matches to the bolometric light curve and expansion-velocity data on the plateau. The progenitor models were selected from a pre-existing grid¹⁰¹ of MESA^{102, 103, 104, 105, 106} RSG progenitor models with expected ejecta masses and radii within the family of explosions consistent with the L_{50} , t_p , and M_{Ni} of SN 2018zd (Extended Data Fig. 6). All models began at solar metallicity ($Z = 0.02$), and the naming scheme gives explosion properties (M[M_{ej}/M_{\odot}]-R[R/R_{\odot}]-E[$E_{\text{exp}}/10^{51}$ erg]). The high-ejecta-mass model, M17.2_R718_E0.48, is $18.8 M_{\odot}$ at core collapse ($20 M_{\odot}$ at Zero Age Main Sequence (ZAMS)) with no rotation, no exponential overshooting ($f_{\text{ov}} = f_{0,\text{ov}} = 0.0$), mixing length $\alpha_{\text{env}} = 2.0$ in the H-rich envelope, and a wind efficiency factor $\eta_{\text{wind}} = 0.4$. The moderate model, M14.5_R864_E0.37, is $16.3 M_{\odot}$ at core collapse ($17 M_{\odot}$ at ZAMS) with modest initial rotation $\Omega/\Omega_{\text{crit}} = 0.2$, no exponential overshooting, $\alpha_{\text{env}} = 2.0$, and $\eta_{\text{wind}} = 0.2$. The low-ejecta-mass and large-radius model, M8.3_R1035_E0.23, is $11.8 M_{\odot}$ at core collapse ($15 M_{\odot}$ at ZAMS) with modest rotation $\Omega/\Omega_{\text{crit}} = 0.2$, moderately high exponential overshooting ($f_{\text{ov}} = 0.018, f_{0,\text{ov}} = 0.006$), $\alpha_{\text{env}} = 2.0$, and $\eta_{\text{wind}} = 0.9$. Despite the ZAMS mass typical of a red supergiant, this model sufficiently captures the relevant explosion properties for the SAGB explosion scenario, as the mass of the H-rich ejecta, explosion energy, and progenitor radius determine the plateau properties of Type II-P SNe, not the ZAMS mass.

The explosion energies for each model were then chosen and adjusted to match the light curve of SN 2018zd with the respective progenitor model radii using the degeneracy relations⁷²

$$\begin{aligned}\log(E_{51}) &= -0.728 + 2.148 \log(L_{p,42}) - 0.280 \log(M_{\text{Ni}}) + 2.091 \log(t_{p,2}) - 1.632 \log(R_{500}), \\ \log(M_{10}) &= -0.947 + 1.474 \log(L_{p,42}) - 0.518 \log(M_{\text{Ni}}) + 3.867 \log(t_{p,2}) - 1.120 \log(R_{500}),\end{aligned}\tag{1}$$

where $E_{51} = E_{\text{exp}}/10^{51}$ erg, $M_{10} = M_{\text{ej}}/10 M_{\odot}$, M_{Ni} is in units of M_{\odot} , $L_{p,42} = L_{50}/10^{42}$ erg s⁻¹, $t_{p,2} = t_p/100$ d, and $R_{500} = R/500 R_{\odot}$. Plugging in $L_{50} = 8.6 \times 10^{41}$ erg s⁻¹ from the bolometric light curve at day 50, $t_p = 125.4$ d determined by fitting the drop from the plateau¹⁶, and observed $M_{\text{Ni}} = 0.0086 M_{\odot}$, these relations describe the possible explosion parameter space (Extended Data Fig. 6). These relations are intended for Ni-rich ($M_{\text{Ni}} > 0.03 M_{\odot}$) Type II-P SNe of RSG progenitors with no fallback, but nonetheless provide a heuristic estimate for the degeneracy between explosion energy, progenitor radius, and ejected mass.

This degeneracy motivates the set of progenitor models and explosion energies which we use to reproduce the light-curve properties, and reveals low recovered E_{exp} which overlap significantly with the expected parameter space of ECSNe. The mapping between M_{ej} recovered for Fe CCSNe and ECSNe is less robust, as differences in mixing extent and H/He abundances could account for differences in the recovered M_{ej} from explosions of different stellar progenitors^{71, 107, 72}. As seen in Extended Data Fig. 6, even though SN 2018zd is not particularly dim, low-energy explosions of radially extended progenitors can match the plateau luminosity. A slightly lower- M_{ej} progenitor with a radius of $1400 R_{\odot}$, for example, could even produce this luminosity with an explosion energy of $\approx 1.5 \times 10^{50}$ erg.

The explosions were carried out using MESA revision 12115, making use of the updated prescription for removing material falling back onto the inner boundary^{106, 72}, which can be relevant at the low explosion energies required here. Of the three explosions, only M8.3_R1035_E0.23 undergoes significant late-time fallback, totaling $2 M_{\odot}$, which is excised from the model with no extra heating and negligible change in the total explosion energy. A thermal bomb was injected in the innermost $0.1 M_{\odot}$ of each model, heating the star to the desired total final energy E_{exp} . The evolution of the shock was modeled in MESA with the ‘‘Duffell RTI’’ prescription for mixing via the Rayleigh-Taylor instability^{108, 105}, terminating near shock breakout, when the shock reaches a mass coordinate of $0.04 M_{\odot}$ below the outer boundary of each model. The ^{56}Ni distribution in each model was then scaled to match the observed value of $0.0086 M_{\odot}$.

These models near shock breakout were then handed off to STELLA^{109, 110, 111} to produce synthetic observables. Bolometric light curves and expansion velocities were produced using 600 spatial zones and 100 frequency bins, without any additional material outside the stellar photosphere (Extended Data Fig. 6). We see good agreement between all three models and observations (varying by at least 50% in M_{ej} , E_{exp} , and R), with deviations at early times which can be attributed to the extended stellar atmosphere and potential interaction with the circumstellar environment.

In order to account for the early deviations, we affix a wind density profile with $\rho_{\text{wind}}(r) = \dot{M}_{\text{wind}}/4\pi r^2 v_{\text{wind}}$, where \dot{M}_{wind} is a constant wind mass-loss rate, and v_{wind} is the wind velocity for time t_{wind} (i.e., $M_{\text{wind}} = \dot{M}_{\text{wind}} t_{\text{wind}}$), onto the MESA model at handoff to STELLA. For models with CSM, 600 zones are used in STELLA, including 400 zones for the original ejecta, and 200 additional zones for the wind model. We construct a grid of CSM models by varying the following

parameters: $\dot{M}_{\text{wind}} = \{10^{-4}, 3 \times 10^{-4}, 10^{-3}, 3 \times 10^{-3}, 10^{-2}, 3 \times 10^{-2}, 10^{-1}, 3 \times 10^{-1}\} M_{\odot} \text{ yr}^{-1}$ and $t_{\text{wind}} = \{1, 3, 10, 30\} \text{ yr}$ for each MESA model, assuming a typical wind velocity¹⁸ $v_{\text{wind}} = 20 \text{ km s}^{-1}$. Then we perform χ^2 fitting on the observed bolometric light curve over the full temporal evolution and find the best-fit parameters $\dot{M}_{\text{wind}} = 0.01 M_{\odot} \text{ yr}^{-1}$ and $t_{\text{wind}} = 10 \text{ yr}$.

Remarkably, the best-fit parameters are the same for all three degenerate models, and also reproduce the early blueward UV-colour evolution (Extended Data Fig. 6). Thus, we choose M8.3_R1035_E0.23 as a representative model and present it for the UV-colour plot in Figure 2. In addition to matching the early-time luminosity excess, a dense wind profile suppresses the early photospheric and Fe line velocities²⁰. The kink seen in the modeled Fe line velocity with Sobolev optical depth $\tau_{\text{Sob}} = 1$ in the STELLA models can be attributed to numerics at the boundary between the CSM profile and the surface of the stellar ejecta (Extended Data Fig. 6). Overall the models still yield general agreement between the calculated velocity evolution and the data.

We note that between 3–10 d after the explosion, the blackbody temperatures ($\sim 20,000\text{--}25,000 \text{ K}$) may be underestimated (see Section Follow-up imaging), which could affect the luminosity around the peak, and so the CSM models. For the flash spectral model comparisons in Figure 3, we use a conservative temperature constraint of $\sim 20,000\text{--}30,000 \text{ K}$.

Alternative scenarios. A low-mass ($\lesssim 9.6 M_{\odot}$) Fe CCSN is a possible alternative for SN 2018zd, as similar explosion energy ($\sim 10^{50} \text{ erg}$)¹¹² and nucleosynthesis¹¹³ to ECSNe may be expected because of a similar steep density gradient outside the degenerate core. For a low-mass RSG star, however, no high constant ($\gtrsim 10^{-5} M_{\odot} \text{ yr}^{-1}$)^{114, 115, 116} and/or eruptive^{117, 118} mass loss is expected

to produce dense confined He-, C-, and N-rich, but O-poor CSM (but note that the mass loss is quite sensitive to the model treatments of, e.g., convection and off-center nuclear burning¹¹⁹). In addition, a low-mass RSG has Si-, O-, and He-rich layers⁵ which are expected to produce additional Si, S, Ca, Mg, O, C, and He lines in nebular spectra¹¹. Thus, a low-mass Fe CCSN may be able to explain the light-curve morphology, but likely not the early-time CSM interaction and nebular spectra observed for SN 2018zd.

On the other side of the progenitor mass spectrum, another possible alternative for SN 2018zd is a high-mass ($\gtrsim 25 M_{\odot}$) Fe CCSN, as small kinetic energy ($\sim 10^{50}$ erg) and ejected radioactive ^{56}Ni mass ($\lesssim 10^{-3} M_{\odot}$) may be expected owing to fallback accretion onto the central remnant^{120, 121}. For such high fallback accretion, however, extra luminosity ($L \propto t^{-5/3}$) at late times ($t \gtrsim 200$ d) is expected^{122, 123}. Also, no ejected stable ^{58}Ni should be observed, as produced in the innermost neutron-rich layer¹⁰. Thus, a high-mass Fe CCSN may be able to explain the photospheric light curve, but not the late-time exponential tail and nebular spectra of SN 2018zd.

If the luminosity distance to NGC 2146 were larger than 12 Mpc, it would be quite unlikely that SN 2018zd is an ECSN, since $M_{\text{Ni}} > 0.01 M_{\odot}$, $E_{\text{exp}} > 4 \times 10^{50}$ erg, and $M_{\text{ej}} > 10 M_{\odot}$ in a reasonable progenitor radius range of 400–1400 R_{\odot} according to the light-curve scaling (Eq. 1). Then SN 2018zd would become a real challenge to stellar evolution and SN explosion theories to reconcile all of the observational ECSN indicators with a higher M_{Ni} , E_{exp} , M_{ej} , and M_{ZAMS} for the progenitor. If the luminosity distance were 18 Mpc, the progenitor candidate detection of SN 2018zd in *HST* F814W would become as bright as that of the SN 2005cs progenitor (Extended Data Fig. 2), but still on the faint end of Type II SN progenitors^{117, 124} despite the expected higher

M_{ej} and M_{ZAMS} from the light-curve scaling.

Other ECSN candidates. In addition to SN 1054, other previously suggested ECSN candidates can be divided into three types: intermediate-luminosity red transients (ILRTs; e.g., SN 2008S and AT 2017be)^{125, 126, 127, 128, 129, 130}; low-luminosity Type II-P SNe^{7, 8, 17, 38}; and Type IIn-P SNe (e.g., SNe 2009kn and 2011ht)^{131, 132, 18, 29} (Extended Data Table 1).

ILRTs are the luminosity gap transients between novae and supernovae, whose origin has been debated as either a massive star outburst^{133, 134, 135, 136} or terminal ECSN explosion^{125, 126, 127, 128, 129, 130}. Their progenitors are surrounded by dusty, optically thick shells, resulting in CSM-dominated transients^{125, 126, 127, 133, 134, 128}. However, their faint light-curve morphology with CSM interaction requires extremely low explosion energy ($\lesssim 10^{48}$ erg) that is unexpected for ECSNe^{9, 18, 137}, and their chemical composition and nucleosynthesis are unclear owing to the lack of nebular-phase spectra.

Low-luminosity Type II-P SNe typically yield low ^{56}Ni mass ($\lesssim 10^{-2} M_{\odot}$)¹⁷ with ECSN-like light-curve morphology (Fig. 1), but their chemical composition and nucleosynthesis are inconsistent with ECSNe¹¹ (Extended Data Fig. 7), and their CSM density is generally low compared to that expected from ECSNe^{4, 18} (except for SN 2016bkv³⁸). Low-mass RSG progenitors have been directly identified for SNe 2003gd¹³⁸, 2005cs^{139, 138}, 2008bk¹⁴⁰, excluding SAGB stars – the progenitors of ECSNe.

Type IIn-P SNe show Type IIn-like narrow CSM emission lines in spectra and Type II-P-like light-curve morphology with large plateau drops similar to ECSNe^{131, 132, 29, 18} (Extended Data

Fig. 8), although the SN signatures (e.g., chemical abundance) are mostly hidden below the CSM interaction. Whilst no Type IIn-P SN progenitors have been directly identified, a pre-explosion outburst has been observed for SN 2011ht¹⁴¹. The true nature of Type IIn-P SNe is yet to be revealed.

The rate of ECSNe. Since Type IIn-P SNe share similar properties as SN 2018zd, the Type IIn-P SN rate may be related to the ECSN rate. As there is no rate estimation for Type IIn-P SNe in the literature to our knowledge, we put a rough lower limit using publicly announced Type IIn SNe on WISEREP and/or the Transient Name Server (TNS¹⁴²) by cross-checking with the literature and the Open Supernova Catalog and cross-correlating the public spectra to SN spectral libraries Superfit¹⁴³ and SNID¹⁴⁴ when available. There are 528 objects classified as Type IIn SNe on WISEREP and/or TNS (as of 2020 Mar. 11). We exclude 73 objects as misclassified early-flash Type II SNe, Type Ia-CSM SNe, Type Ibn SNe, SN imposters, or active galactic nuclei. Although 241 objects do not have enough public and/or published spectra and/or light curves to secure the Type IIn classifications and/or to be identified as Type IIn-P SNe, we include them in the further analysis so that we do not overestimate the lower limit (Extended Data Fig. 8).

To identify Type IIn-P SN candidates from the 455 objects, we apply two light-curve criteria based on the known Type IIn-P SN characteristics: (1) the V , r/R , or i/I -band decline of less than 2 mag in the first 50 d after the explosion; and (2) the V , r/R , or i/I -band drop of more than 2 mag in 30 d within 100–150 d after the explosion. This yields four Type IIn-P SN candidates: SNe 2005cl ($z = 0.025878$)¹⁴⁵; 2005db ($z = 0.015124$)¹⁴⁵; 2006bo ($z = 0.0153$)¹⁴⁶; and 2011A ($z = 0.008916$)¹⁴⁷, in addition to three known Type IIn-P SNe 1994W ($z = 0.004116$)¹⁴⁸, 2009kn

($z = 0.015798$)¹³¹, and 2011ht ($z = 0.003646$)¹³² (Extended Data Fig. 8).

To compare with the volume-limited (≤ 60 Mpc) Lick Observatory Supernova Search (LOSS) sample^{149, 150}, we apply the same distance cut, leaving 42 Type II_n SNe (17 and 25 with sufficient and insufficient data, respectively) and 3 Type II_n-P SNe 1994W, 2011A, and 2011ht. As these SNe were discovered by different surveys with different strategies, we have no handle on the incompleteness (but see Extended Data Fig. 8). Thus, we neglect the incompleteness and take the number ratio of Type II_n-P to Type II_n SNe within 60 Mpc multiplied by the LOSS Type II_n SN rate¹⁵⁰, $3/42 \times 8.8\% = 0.63\%$ of all CCSNe, as a rough lower limit of the Type II_n-P SN rate.

The identification of SN 2018zd-like SNe from Type II-P SNe (48.2% of all CCSNe) requires not only the light-curve morphology, but also the early UV colours and the flash and nebular spectroscopy, all of which combined are rarely available on WISEREP, TNS, and/or the Open Supernova Catalog. This current sample limitation may indicate that many SN 2018zd-like SNe have been overlooked as normal Type II-P SNe. Given the limitation, we simply take the lowest possible limit of $> 0\%$ with the at least one identification of SN 2018zd as an ECSN.

By combining the estimated Type II_n-P and SN 2018zd-like lower limits, we obtain a Type II_n-P + SN 2018zd-like lower limit of $> 0.6\%$ of all CCSNe. From the nucleosynthetic point of view, ECSNe are expected to constitute $\lesssim 8.5\%$ of all CCSNe¹¹³. With the above estimates, the ECSN rate can be roughly constrained within 0.6–8.5% of all CCSNe, which corresponds to a narrow SAGB progenitor mass window of $\Delta M_{\text{SAGB}} \approx 0.06\text{--}0.69 M_{\odot}$ assuming maximum and minimum SAGB masses of $9.25 M_{\odot}$ and $9.25 M_{\odot} - \Delta M_{\text{SAGB}}$ (respectively) at solar metallicity⁴ (Extended

Data Fig. 9). We note that Type II_n-P and SN 2018zd-like rates are likely metallicity dependent (as is the SAGB mass window), but we defer more detailed analysis with a homogeneous sample in the future when one becomes publicly available, potentially putting stringent constraints on many fields of physics and astrophysics.

40. Brown, T. M. *et al.* Las Cumbres Observatory Global Telescope Network. *Publications of the Astronomical Society of the Pacific* **125**, 1031 (2013).
41. Stetson, P. B. Homogeneous Photometry for Star Clusters and Resolved Galaxies. II. Photometric Standard Stars. *Publications of the Astronomical Society of the Pacific* **112**, 925–931 (2000).
42. Albareti, F. D. *et al.* The 13th Data Release of the Sloan Digital Sky Survey: First Spectroscopic Data from the SDSS-IV Survey Mapping Nearby Galaxies at Apache Point Observatory. *Astrophys. J. Supplements* **233**, 25 (2017).
43. Brown, P. J., Breeveld, A. A., Holland, S., Kuin, P. & Pritchard, T. SOUSA: the Swift Optical/Ultraviolet Supernova Archive. *Ap&SS* **354**, 89–96 (2014).
44. Breeveld, A. A. *et al.* An Updated Ultraviolet Calibration for the Swift/UVOT. In McEnery, J. E., Racusin, J. L. & Gehrels, N. (eds.) *American Institute of Physics Conference Series*, vol. 1358 of *American Institute of Physics Conference Series*, 373–376 (2011).
45. Raab, H. Astrometrica: Astrometric data reduction of CCD images (2012).

46. Zacharias, N. *et al.* The Fourth US Naval Observatory CCD Astrograph Catalog (UCAC4). *Astron. J.* **145**, 44 (2013).
47. Yaron, O. & Gal-Yam, A. WISeREP—An Interactive Supernova Data Repository. *Publications of the Astronomical Society of the Pacific* **124**, 668 (2012). <https://wiserep.weizmann.ac.il/>.
48. Guillochon, J., Parrent, J., Kelley, L. Z. & Margutti, R. An Open Catalog for Supernova Data. *Astrophys. J.* **835**, 64 (2017).
49. Oke, J. B. *et al.* The Keck Low-Resolution Imaging Spectrometer. *Publications of the Astronomical Society of the Pacific* **107**, 375 (1995).
50. McCarthy, J. K. *et al.* Blue channel of the Keck low-resolution imaging spectrometer, vol. 3355 of *Society of Photo-Optical Instrumentation Engineers (SPIE) Conference Series*, 81–92 (Optical Astronomical Instrumentation, 1998).
51. Rockosi, C. *et al.* The low-resolution imaging spectrograph red channel CCD upgrade: fully depleted, high-resistivity CCDs for Keck, vol. 7735 of *Society of Photo-Optical Instrumentation Engineers (SPIE) Conference Series*, 77350R (Optical Astronomical Instrumentation, 2010).
52. Faber, S. M. *et al.* The DEIMOS spectrograph for the Keck II Telescope: integration and testing, vol. 4841 of *Society of Photo-Optical Instrumentation Engineers (SPIE) Conference Series*, 1657–1669 (2003).

53. Filippenko, A. V. The importance of atmospheric differential refraction in spectrophotometry. *Publications of the Astronomical Society of the Pacific* **94**, 715–721 (1982).
54. Valenti, S. *et al.* The first month of evolution of the slow-rising Type IIP SN 2013ej in M74. *Mon. Not. R. Astron. Soc.* **438**, L101–L105 (2014).
55. Perley, D. A. Fully Automated Reduction of Longslit Spectroscopy with the Low Resolution Imaging Spectrometer at the Keck Observatory. *Publications of the Astronomical Society of the Pacific* **131**, 084503 (2019).
56. Horne, K. An optimal extraction algorithm for CCD spectroscopy. *Publications of the Astronomical Society of the Pacific* **98**, 609–617 (1986).
57. Jerkstrand, A. *et al.* Supersolar Ni/Fe production in the Type IIP SN 2012ec. *Mon. Not. R. Astron. Soc.* **448**, 2482–2494 (2015).
58. Schmidt, G. D., Stockman, H. S. & Smith, P. S. Discovery of a Sub-Megagauss Magnetic White Dwarf through Spectropolarimetry. *Astrophys. J. Letters* **398**, L57 (1992).
59. Serkowski, K., Mathewson, D. S. & Ford, V. L. Wavelength dependence of interstellar polarization and ratio of total to selective extinction. *Astrophys. J.* **196**, 261–290 (1975).
60. Schlafly, E. F. & Finkbeiner, D. P. Measuring Reddening with Sloan Digital Sky Survey Stellar Spectra and Recalibrating SFD. *Astrophys. J.* **737**, 103 (2011).
61. NASA/IPAC Infrared Science Archive. <https://irsa.ipac.caltech.edu/applications/DUST/>.

62. Jester, S. *et al.* The Sloan Digital Sky Survey View of the Palomar-Green Bright Quasar Survey. *Astron. J.* **130**, 873–895 (2005).
63. Leonard, D. C. *et al.* The Distance to SN 1999em in NGC 1637 from the Expanding Photosphere Method. *Publications of the Astronomical Society of the Pacific* **114**, 35–64 (2002).
64. Leonard, D. C. *et al.* A Study of the Type II-Plateau Supernova 1999gi and the Distance to its Host Galaxy, NGC 3184. *Astron. J.* **124**, 2490–2505 (2002).
65. Bose, S. *et al.* Supernova 2012aw - a high-energy clone of archetypal Type IIP SN 1999em. *Mon. Not. R. Astron. Soc.* **433**, 1871–1891 (2013).
66. Van Dyk, S. D. *et al.* The Type II-plateau Supernova 2017eaw in NGC 6946 and Its Red Supergiant Progenitor. *Astrophys. J.* **875**, 136 (2019).
67. Fitzpatrick, E. L. Correcting for the Effects of Interstellar Extinction. *Publications of the Astronomical Society of the Pacific* **111**, 63–75 (1999).
68. Dessart, L. & Hillier, D. J. Distance determinations using type II supernovae and the expanding photosphere method. *Astron. Astrophys.* **439**, 671–685 (2005).
69. Polshaw, J. *et al.* A supernova distance to the anchor galaxy NGC 4258. *Astron. Astrophys.* **580**, L15 (2015).
70. Hamuy, M. & Pinto, P. A. Type II Supernovae as Standardized Candles. *Astrophys. J. Letters* **566**, L63–L65 (2002).

71. Kasen, D. & Woosley, S. E. Type II Supernovae: Model Light Curves and Standard Candle Relationships. *Astrophys. J.* **703**, 2205–2216 (2009).
72. Goldberg, J. A., Bildsten, L. & Paxton, B. Inferring Explosion Properties from Type II-Plateau Supernova Light Curves. *Astrophys. J.* **879**, 3 (2019).
73. Beaton, R. L. *et al.* Old-Aged Primary Distance Indicators. *SS Rev.* **214**, 113 (2018).
74. Taramopoulos, A., Payne, H. & Briggs, F. H. HI observations of the starburst galaxy NGC 2146. *Astron. Astrophys.* **365**, 360–369 (2001).
75. Tang, Q.-W., Wang, X.-Y. & Tam, P.-H. T. Discovery of GeV Emission from the Direction of the Luminous Infrared Galaxy NGC 2146. *Astrophys. J.* **794**, 26 (2014).
76. Armus, L., Heckman, T. M., Weaver, K. A. & Lehnert, M. D. ROSAT Observations of NGC 2146: Evidence for a Starburst-driven Superwind. *Astrophys. J.* **445**, 666 (1995).
77. Kreckel, K. *et al.* A Far-IR View of the Starburst-driven Superwind in NGC 2146. *Astrophys. J.* **790**, 26 (2014).
78. Skibba, R. A. *et al.* The Emission by Dust and Stars of Nearby Galaxies in the Herschel KINGFISH Survey. *Astrophys. J.* **738**, 89 (2011).
79. Tarchi, A. *et al.* Radio supernovae, supernova remnants and H II regions in NGC 2146 observed with MERLIN and the VLA. *Astron. Astrophys.* **358**, 95–103 (2000).
80. Aniano, G. *et al.* Modeling Dust and Starlight in Galaxies Observed by Spitzer and Herschel: The KINGFISH Sample. *Astrophys. J.* **889**, 150 (2020).

81. NASA/IPAC Extragalactic Database. <http://ned.ipac.caltech.edu/>.
82. Dolphin, A. DOLPHOT: Stellar photometry (2016).
83. Zhang, K. & Bloom, J. S. deepCR: Cosmic Ray Rejection with Deep Learning. *Astrophys. J.* **889**, 24 (2020).
84. Fazio, G. G. *et al.* The Infrared Array Camera (IRAC) for the Spitzer Space Telescope. *Astrophys. J. Supplements* **154**, 10–17 (2004).
85. Rieke, G. H. *et al.* The Multiband Imaging Photometer for Spitzer (MIPS). *Astrophys. J. Supplements* **154**, 25–29 (2004).
86. Makovoz, D., Roby, T., Khan, I. & Booth, H. *MOPEX: a software package for astronomical image processing and visualization*, vol. 6274 of *Society of Photo-Optical Instrumentation Engineers (SPIE) Conference Series*, 62740C (2006).
87. Makovoz, D. & Marleau, F. R. Point-Source Extraction with MOPEX. *Publications of the Astronomical Society of the Pacific* **117**, 1113–1128 (2005).
88. IRAC Instrument and Instrument Support Teams. *IRAC Instrument Handbook* (2015). <https://irsa.ipac.caltech.edu/data/SPITZER/docs/irac/iracinstrumenthandbook/>.
89. MIPS Instrument and MIPS Instrument Support Teams. *MIPS Instrument Handbook* (2011). <https://irsa.ipac.caltech.edu/data/SPITZER/docs/mips/mipsinstrumenthandbook/>.

90. Xue, M. *et al.* A Precise Determination of the Mid-infrared Interstellar Extinction Law Based on the APOGEE Spectroscopic Survey. *Astrophys. J. Supplements* **224**, 23 (2016).
91. Stanway, E. R. & Eldridge, J. J. Re-evaluating old stellar populations. *Mon. Not. R. Astron. Soc.* **479**, 75–93 (2018).
92. Gustafsson, B. *et al.* A grid of MARCS model atmospheres for late-type stars. I. Methods and general properties. *Astron. Astrophys.* **486**, 951–970 (2008).
93. Groenewegen, M. A. T. & Sloan, G. C. Luminosities and mass-loss rates of Local Group AGB stars and red supergiants. *Astron. Astrophys.* **609**, A114 (2018).
94. Tully, R. B. *et al.* The Extragalactic Distance Database. *Astron. J.* **138**, 323–331 (2009).
<http://edd.ifa.hawaii.edu/>.
95. Maund, J. R., Smartt, S. J. & Danziger, I. J. The progenitor of SN 2005cs in the Whirlpool Galaxy. *Mon. Not. R. Astron. Soc.* **364**, L33–L37 (2005).
96. Li, W. *et al.* Identification of the Red Supergiant Progenitor of Supernova 2005cs: Do the Progenitors of Type II-P Supernovae Have Low Mass? *Astrophys. J.* **641**, 1060–1070 (2006).
97. McQuinn, K. B. W., Skillman, E. D., Dolphin, A. E., Berg, D. & Kennicutt, R. The Distance to M51. *Astrophys. J.* **826**, 21 (2016).
98. Dessart, L. & Hillier, D. J. The difficulty of inferring progenitor masses from type-II-Plateau supernova light curves. *Astron. Astrophys.* **625**, A9 (2019).

99. Bersten, M. C., Benvenuto, O. & Hamuy, M. Hydrodynamical Models of Type II Plateau Supernovae. *Astrophys. J.* **729**, 61 (2011).
100. Martinez, L. & Bersten, M. C. Mass discrepancy analysis for a select sample of Type II-Plateau supernovae. *Astron. Astrophys.* **629**, A124 (2019).
101. Goldberg, J. A. & Bildsten, L. The Value of Progenitor Radius Measurements for Explosion Modeling of Type II-Plateau Supernovae. *arXiv e-prints* arXiv:2005.07290 (2020).
102. Paxton, B. *et al.* Modules for Experiments in Stellar Astrophysics (MESA). *Astrophys. J. Supplements* **192**, 3 (2011).
103. Paxton, B. *et al.* Modules for Experiments in Stellar Astrophysics (MESA): Planets, Oscillations, Rotation, and Massive Stars. *Astrophys. J. Supplements* **208**, 4 (2013).
104. Paxton, B. *et al.* Modules for Experiments in Stellar Astrophysics (MESA): Binaries, Pulsations, and Explosions. *Astrophys. J. Supplements* **220**, 15 (2015).
105. Paxton, B. *et al.* Modules for Experiments in Stellar Astrophysics (MESA): Convective Boundaries, Element Diffusion, and Massive Star Explosions. *Astrophys. J. Supplements* **234**, 34 (2018).
106. Paxton, B. *et al.* Modules for Experiments in Stellar Astrophysics (MESA): Pulsating Variable Stars, Rotation, Convective Boundaries, and Energy Conservation. *Astrophys. J. Supplements* **243**, 10 (2019).

107. Kozyreva, A., Nakar, E. & Waldman, R. The role of radioactive nickel in shaping the plateau phase of Type II supernovae. *Mon. Not. R. Astron. Soc.* **483**, 1211–1223 (2019).
108. Duffell, P. C. A One-Dimensional Model for Rayleigh-Taylor Instability in Supernova Remnants. *Astrophys. J.* **821**, 76 (2016).
109. Blinnikov, S. I., Eastman, R., Bartunov, O. S., Popolitov, V. A. & Woosley, S. E. A Comparative Modeling of Supernova 1993J. *Astrophys. J.* **496**, 454–472 (1998).
110. Blinnikov, S., Lundqvist, P., Bartunov, O., Nomoto, K. & Iwamoto, K. Radiation Hydrodynamics of SN 1987A. I. Global Analysis of the Light Curve for the First 4 Months. *Astrophys. J.* **532**, 1132–1149 (2000).
111. Blinnikov, S. I. *et al.* Theoretical light curves for deflagration models of type Ia supernova. *Astron. Astrophys.* **453**, 229–240 (2006).
112. Müller, B. *et al.* Three-dimensional simulations of neutrino-driven core-collapse supernovae from low-mass single and binary star progenitors. *Mon. Not. R. Astron. Soc.* **484**, 3307–3324 (2019).
113. Wanajo, S., Müller, B., Janka, H.-T. & Heger, A. Nucleosynthesis in the Innermost Ejecta of Neutrino-driven Supernova Explosions in Two Dimensions. *Astrophys. J.* **852**, 40 (2018).
114. Mauron, N. & Josselin, E. The mass-loss rates of red supergiants and the de Jager prescription. *Astron. Astrophys.* **526**, A156 (2011).

115. Goldman, S. R. *et al.* The wind speeds, dust content, and mass-loss rates of evolved AGB and RSG stars at varying metallicity. *Mon. Not. R. Astron. Soc.* **465**, 403–433 (2017).
116. Beasor, E. R. *et al.* A new mass-loss rate prescription for red supergiants. *Mon. Not. R. Astron. Soc.* **492**, 5994–6006 (2020).
117. Smartt, S. J. Progenitors of Core-Collapse Supernovae. *Ann. Rev. Astron. Astrophys.* **47**, 63–106 (2009).
118. Fuller, J. Pre-supernova outbursts via wave heating in massive stars - I. Red supergiants. *Mon. Not. R. Astron. Soc.* **470**, 1642–1656 (2017).
119. Woosley, S. E. & Heger, A. The Remarkable Deaths of 9-11 Solar Mass Stars. *Astrophys. J.* **810**, 34 (2015).
120. Lisakov, S. M., Dessart, L., Hillier, D. J., Waldman, R. & Livne, E. Progenitors of low-luminosity Type II-Plateau supernovae. *Mon. Not. R. Astron. Soc.* **473**, 3863–3881 (2018).
121. Chan, C., Müller, B., Heger, A., Pakmor, R. & Springel, V. Black Hole Formation and Fallback during the Supernova Explosion of a $40 M_{\odot}$ Star. *Astrophys. J. Letters* **852**, L19 (2018).
122. Dexter, J. & Kasen, D. Supernova Light Curves Powered by Fallback Accretion. *Astrophys. J.* **772**, 30 (2013).

123. Moriya, T. J., Müller, B., Chan, C., Heger, A. & Blinnikov, S. I. Fallback Accretion-powered Supernova Light Curves Based on a Neutrino-driven Explosion Simulation of a $40 M_{\odot}$ Star. *Astrophys. J.* **880**, 21 (2019).
124. Smartt, S. J. Observational Constraints on the Progenitors of Core-Collapse Supernovae: The Case for Missing High-Mass Stars. *Publications of the Astronomical Society of Australia* **32**, e016 (2015).
125. Prieto, J. L. *et al.* Discovery of the Dust-Enshrouded Progenitor of SN 2008S with Spitzer. *Astrophys. J. Letters* **681**, L9 (2008).
126. Botticella, M. T. *et al.* SN 2008S: an electron-capture SN from a super-AGB progenitor? *Mon. Not. R. Astron. Soc.* **398**, 1041–1068 (2009).
127. Thompson, T. A. *et al.* A New Class of Luminous Transients and a First Census of their Massive Stellar Progenitors. *Astrophys. J.* **705**, 1364–1384 (2009).
128. Adams, S. M. *et al.* Almost gone: SN 2008S and NGC 300 2008OT-1 are fainter than their progenitors. *Mon. Not. R. Astron. Soc.* **460**, 1645–1657 (2016).
129. Cai, Y. Z. *et al.* AT 2017be - a new member of the class of intermediate-luminosity red transients. *Mon. Not. R. Astron. Soc.* **480**, 3424–3445 (2018).
130. Stritzinger, M. D. *et al.* The Carnegie Supernova Project II. Observations of the intermediate luminosity red transient SNhunt120. *arXiv e-prints* arXiv:2005.00319 (2020).

131. Kankare, E. *et al.* SN 2009kn - the twin of the Type IIn supernova 1994W. *Mon. Not. R. Astron. Soc.* **424**, 855–873 (2012).
132. Mauerhan, J. C. *et al.* SN 2011ht: confirming a class of interacting supernovae with plateau light curves (Type IIn-P). *Mon. Not. R. Astron. Soc.* **431**, 2599–2611 (2013).
133. Bond, H. E. *et al.* The 2008 Luminous Optical Transient in the Nearby Galaxy NGC 300. *Astrophys. J. Letters* **695**, L154–L158 (2009).
134. Berger, E. *et al.* An Intermediate Luminosity Transient in NGC 300: The Eruption of a Dust-Enshrouded Massive Star. *Astrophys. J.* **699**, 1850–1865 (2009).
135. Smith, N. *et al.* SN 2008S: A Cool Super-Eddington Wind in a Supernova Impostor. *Astrophys. J. Letters* **697**, L49–L53 (2009).
136. Smith, N., Li, W., Silverman, J. M., Ganeshalingam, M. & Filippenko, A. V. Luminous blue variable eruptions and related transients: diversity of progenitors and outburst properties. *Mon. Not. R. Astron. Soc.* **415**, 773–810 (2011).
137. Moriya, T. J. & Eldridge, J. J. Rapidly evolving faint transients from stripped-envelope electron-capture supernovae. *Mon. Not. R. Astron. Soc.* **461**, 2155–2161 (2016).
138. Maund, J. R., Reilly, E. & Mattila, S. A late-time view of the progenitors of five Type IIP supernovae. *Mon. Not. R. Astron. Soc.* **438**, 938–958 (2014).
139. Eldridge, J. J., Mattila, S. & Smartt, S. J. Ruling out a massive asymptotic giant-branch star as the progenitor of supernova 2005cs. *Mon. Not. R. Astron. Soc.* **376**, L52–L56 (2007).

140. Maund, J. R., Mattila, S., Ramirez-Ruiz, E. & Eldridge, J. J. A new precise mass for the progenitor of the Type IIP SN 2008bk. *Mon. Not. R. Astron. Soc.* **438**, 1577–1592 (2014).
141. Fraser, M. *et al.* Detection of an Outburst One Year Prior to the Explosion of SN 2011ht. *Astrophys. J. Letters* **779**, L8 (2013).
142. *Transient Name Server*. <https://wis-tns.weizmann.ac.il/>.
143. Howell, D. A. *et al.* Gemini Spectroscopy of Supernovae from the Supernova Legacy Survey: Improving High-Redshift Supernova Selection and Classification. *Astrophys. J.* **634**, 1190–1201 (2005).
144. Blondin, S. & Tonry, J. L. Determining the Type, Redshift, and Age of a Supernova Spectrum. *Astrophys. J.* **666**, 1024–1047 (2007).
145. Kiewe, M. *et al.* Caltech Core-Collapse Project (CCCP) Observations of Type II_n Supernovae: Typical Properties and Implications for Their Progenitor Stars. *Astrophys. J.* **744**, 10 (2012).
146. Taddia, F. *et al.* Carnegie Supernova Project: Observations of Type II_n supernovae. *Astron. Astrophys.* **555**, A10 (2013).
147. de Jaeger, T. *et al.* SN 2011A: A Low-luminosity Interacting Transient with a Double Plateau and Strong Sodium Absorption. *Astrophys. J.* **807**, 63 (2015).
148. Sollerman, J., Cumming, R. J. & Lundqvist, P. A Very Low Mass of ⁵⁶Ni in the Ejecta of SN 1994W. *Astrophys. J.* **493**, 933–939 (1998).

149. Li, W. *et al.* Nearby supernova rates from the Lick Observatory Supernova Search - II. The observed luminosity functions and fractions of supernovae in a complete sample. *Mon. Not. R. Astron. Soc.* **412**, 1441–1472 (2011).
150. Smith, N., Li, W., Filippenko, A. V. & Chornock, R. Observed fractions of core-collapse supernova types and initial masses of their single and binary progenitor stars. *Mon. Not. R. Astron. Soc.* **412**, 1522–1538 (2011).
151. Arcavi, I. *Hydrogen-Rich Core-Collapse Supernovae*, 239 (Springer, Cham, 2017).
152. Hamuy, M. Observed and Physical Properties of Core-Collapse Supernovae. *Astrophys. J.* **582**, 905–914 (2003).
153. Gutiérrez, C. P. *et al.* Type II Supernova Spectral Diversity. I. Observations, Sample Characterization, and Spectral Line Evolution. *Astrophys. J.* **850**, 89 (2017).
154. Pastorello, A. *et al.* SN 2005cs in M51 - II. Complete evolution in the optical and the near-infrared. *Mon. Not. R. Astron. Soc.* **394**, 2266–2282 (2009).
155. Nakaoka, T. *et al.* The Low-luminosity Type IIP Supernova 2016bkv with Early-phase Circumstellar Interaction. *Astrophys. J.* **859**, 78 (2018).
156. Sukhbold, T., Ertl, T., Woosley, S. E., Brown, J. M. & Janka, H. T. Core-collapse Supernovae from 9 to 120 Solar Masses Based on Neutrino-powered Explosions. *Astrophys. J.* **821**, 38 (2016).

157. Benetti, S. *et al.* The fading of supernova 1997D. *Mon. Not. R. Astron. Soc.* **322**, 361–368 (2001).
158. Van Dyk, S. D. *et al.* Supernova 2008bk and Its Red Supergiant Progenitor. *Astron. J.* **143**, 19 (2012).
159. Maguire, K. *et al.* Constraining the physical properties of Type II-Plateau supernovae using nebular phase spectra. *Mon. Not. R. Astron. Soc.* **420**, 3451–3468 (2012).
160. Humphreys, R. M. *et al.* The Unusual Temporal and Spectral Evolution of SN2011ht. II. Peculiar Type IIn or Impostor? *Astrophys. J.* **760**, 93 (2012).

Acknowledgements We are grateful to A. Suzuki, T. Takiwaki, T. Nozawa, M. Tanaka, C. Kobayashi, R. Ouchi, T. Matsuoka, T. Hayakawa, S. I. Blinnikov, K. Chen, L. Bildsten, and B. Paxton for comments and discussions, to C. P. Gutiérrez and A. Pastorello for sharing the velocity data of the Type II SN sample and SN 2005cs (respectively), and to Peter Iláš for creating the colour-composite image.

D. Hiramatsu, D.A.H., G.H., C.M., and J.B. were supported by NSF grants AST-1313484 and AST-1911225, as well as by NASA grant 80NSSC19kf1639. D. Hiramatsu is thankful for support and hospitality by the Kavli Institute for the Physics and Mathematics of the Universe (IPMU) where many discussions of this work took place. J.A.G. is supported by the NSF GRFP under grant number 1650114. K.M. acknowledges support by JSPS KAKENHI grants 20H00174, 20H04737, 18H04585, 18H05223, and 17H02864. K.N.’s work and D. Hiramatsu’s visit to Kavli IPMU have been supported by the World Premier International Research Center Initiative (WPI Initiative), MEXT, and JSPS KAKENHI grants JP17K05382 and JP20K04024, Japan. I.A. is a CIFAR Azrieli Global Scholar in the Gravity and the Extreme Universe Program and acknowledges

support from that program, from the Israel Science Foundation (grant numbers 2108/18 and 2752/19), from the United States - Israel Binational Science Foundation (BSF), and from the Israeli Council for Higher Education Alon Fellowship. Research by K.A.B., S.V., and Y.D. is supported by NSF grant AST-1813176. J.E.A. and N.S. receive support from NSF grant AST-1515559. Research by D.J.S. is supported by NSF grants AST-1821967, 1821987, 1813708, 1813466, and 1908972. G.S.A. acknowledges support from the Infrared Processing and Analysis Center (IPAC) Visiting Graduate Student Fellowship and from NASA/*HST* grant SNAP-15922 from the Space Telescope Science Institute (STScI), which is operated by the Association of Universities for Research in Astronomy (AURA), Inc., under NASA contract NAS5-26555. A.V.F. is grateful for financial assistance from the Christopher R. Redlich Fund, the TABASGO Foundation, and the Miller Institute for Basic Research in Science (U.C. Berkeley); additional funding was provided by NASA/*HST* grant AR-14295 from STScI. G.F. acknowledges the support from CONICET through grant PIP-2015-2017-11220150100746CO and from ANPCyT through grant PICT-2017-3133.

This paper made use of data from the Las Cumbres Observatory global network of telescopes through the Global Supernova Project. Some of the observations reported herein were obtained at the Bok 2.3m telescope, a facility of the University of Arizona, at the MMT Observatory, a joint facility of the University of Arizona and the Smithsonian Institution, and at the W. M. Keck Observatory which is operated as a scientific partnership among the California Institute of Technology, the University of California, and NASA; the observatory was made possible by the generous financial support of the W. M. Keck Foundation. This work is partly based on observations made with the NASA/ESA *Hubble Space Telescope*, obtained from the Data Archive at STScI. These observations are associated with programs GO-9788, GO-13007, and GO-15151. Financial support for program GO-15151 was provided by NASA through a grant from STScI. This work is based in part on observations made with the *Spitzer Space Telescope*, which is operated by the Jet Propulsion Laboratory, California Institute of Technology under a contract with NASA. This research has

made use of the NASA/IPAC Extragalactic Database (NED), which is funded by the National Aeronautics and Space Administration and operated by the California Institute of Technology. We thank the support of the staffs at the Neil Gehrels *Swift* Observatory.

The authors wish to recognise and acknowledge the very significant cultural role and reverence that the summits of Maunakea and Haleakalā have always had within the indigenous Hawaiian community. We are most fortunate to have the opportunity to conduct observations from these mountains.

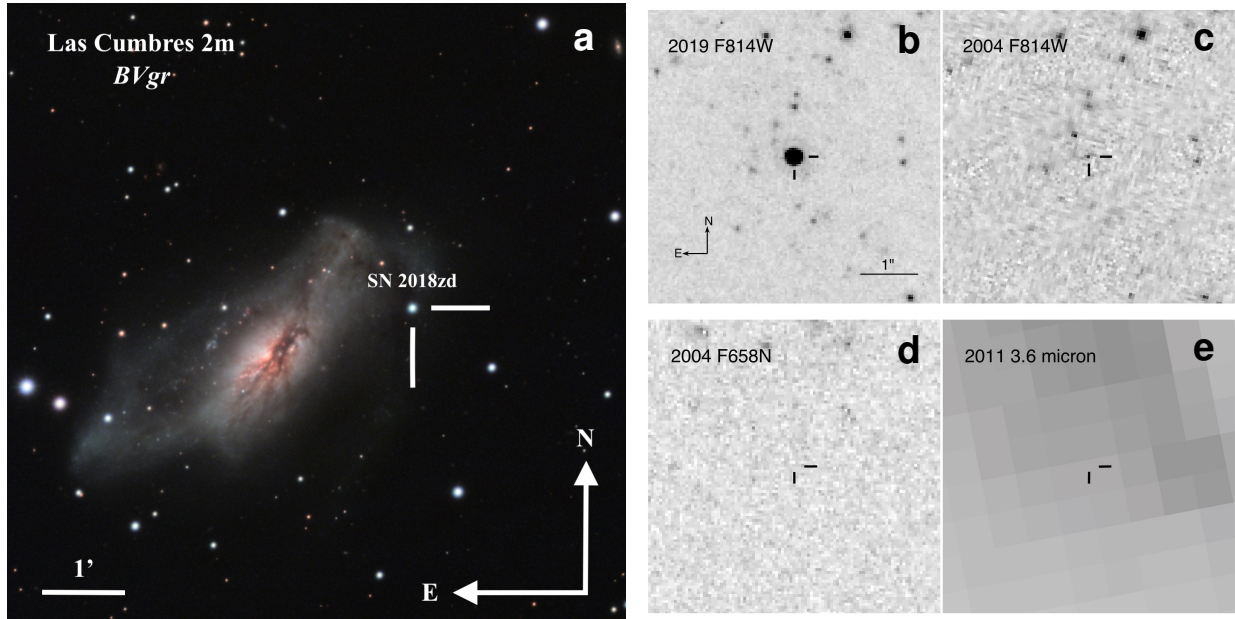
Author Contributions D. Hiramatsu initiated the study, triggered follow-up observations, reduced the Las Cumbres data, produced the light-curve models, performed the analysis, and wrote the manuscript. D.A.H. is the PI of the Las Cumbres Observatory Global Supernova Project through which all of the Las Cumbres data were obtained; he also assisted with data interpretations and the manuscript. S.D.V.D. is the PI of the *HST* program “The Stellar Origins of Supernovae” (GO-15151) through which the post-explosion *HST* data were obtained; he also found the progenitor candidate in the pre-explosion *HST* F814W image, calculated the upper limits in the pre-explosion *HST* and *Spitzer* images, and assisted with data interpretations and the manuscript. J.A.G. produced the progenitor and light-curve models and assisted with their interpretations and the manuscript. K.M. assisted with theoretical nebular spectral model interpretations and the manuscript. T.J.M. and N.T. assisted with theoretical SAGB progenitor and ECSN light-curve model interpretations and the manuscript. K.N. assisted with theoretical SAGB progenitor and ECSN explosion model interpretations and the manuscript. G.H. assisted in obtaining the Las Cumbres data, reduced the FLOYDS spectra, and contributed comments to the manuscript. I.A., C.M., and J.B. assisted in obtaining the Las Cumbres data; I.A. and C.M. also contributed comments to the manuscript. K.A.B. obtained the Keck LRIS and DEIMOS spectra, reduced the LRIS spectra, and contributed comments to the manuscript. S.V. is the PI of the Keck proposals (2018B, project code U009; 2019A, project code U019; 2019B, project

code U034) under which the nebular spectra were obtained; he also built the Las Cumbres photometric and spectroscopic reduction pipelines, reduced the Keck DEIMOS spectrum, and contributed comments to the manuscript. Y.D. assisted in obtaining the Keck LRIS and DEIMOS spectra. P.J.B. obtained and reduced the *Swift* UVOT data. J.E.A. obtained and reduced the MMT and Bok spectra. C.B. reduced and analysed the MMT SPOL spectropolarimetry. G.G.W. is the PI of the Supernova Spectropolarimetry (SNSPOL) project. P.S.S. is the PI of the SPOL instrument. G.G.W. and P.S.S. collected the spectropolarimetric data with the SPOL instrument at the MMT Observatory. N.S. is the PI of the MMT and Bok programs; he also contributed comments to the manuscript. D.J.S. co-leads the University of Arizona team that obtained the MMT and Bok spectra; he also contributed comments to the manuscript. G.S.A. reduced and analysed the archival *HST* WFC3/IR data (GO-12206) of the host galaxy NGC 2146. C.X. and C.M. analysed and rejected the cosmic rays in the pre-explosion *HST* F814W image. A.V.F., M.C.B., G.F., and P.L.K. are Co-Is of the *HST* program (GO-15151); they also contributed comments to the manuscript. T.N. monitored the supernova and provided his photometry. K.I. is the discoverer of the supernova; he also monitored the supernova and provided his photometry.

Author Information Reprints and permissions information is available at www.nature.com/reprints. The authors declare that they have no competing financial interests. Correspondence and requests for materials should be addressed to D. Hiramatsu (dhiramatsu@lco.global).

Data Availability The photometric and spectroscopic data that support the findings of this study will be available on the Open Supernova Catalog at <https://sne.space/> and WISeREP at <https://wiserep.weizmann.ac.il/>. Source Data for Figs. 1 & 2, and for Extended Data Figs. 2, 5, & 6 will be provided with the online version of the paper.

Extended Data

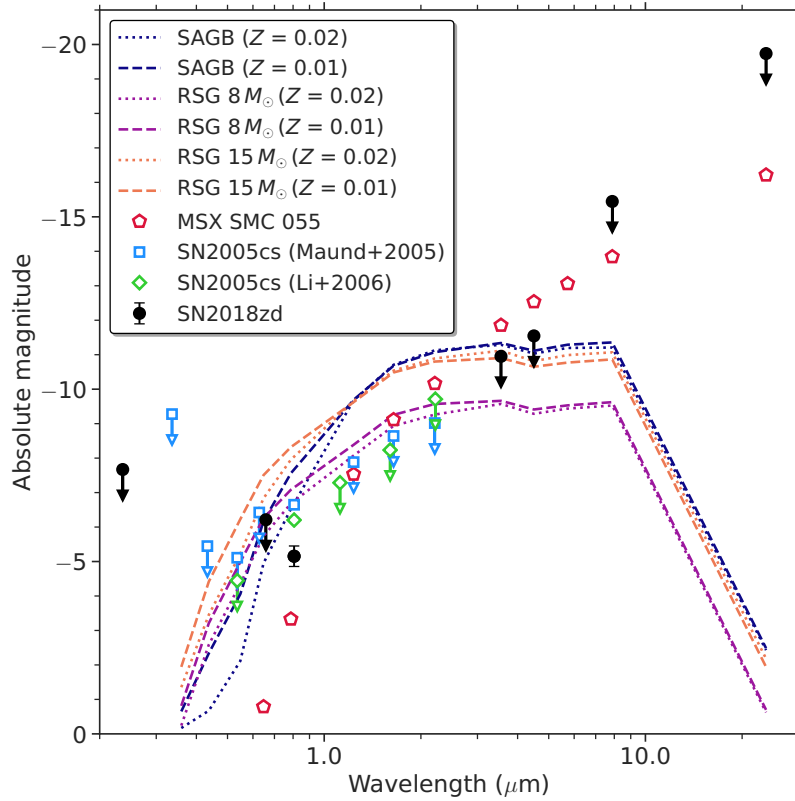


Extended Data Figure 1 The host galaxy and post- and pre-explosion images of SN 2018zd.

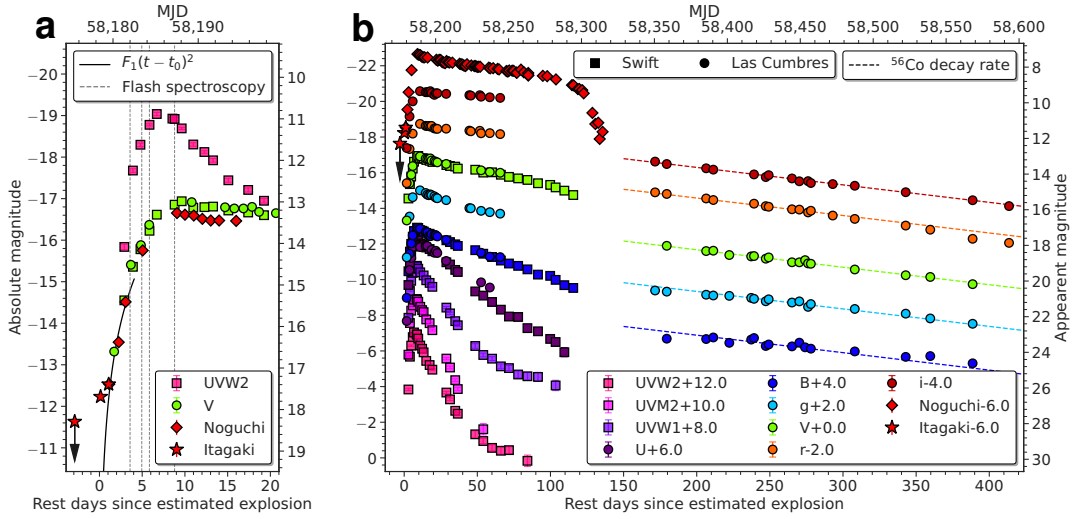
(a) Las Cumbres 2 m *BVgr*-composite image of SN 2018zd and the host starburst galaxy NGC 2146, courtesy of Peter Iláš. At the assumed luminosity distance of 9.6 Mpc, 1' corresponds to 2.8 kpc. SN 2018zd is on a tidal stream which was likely ejected during a galaxy merger event⁷⁴.

(b) Portion of an *HST* WFC3/UVIS F814W mosaic obtained on 2019 May 19, 443.7 d after the explosion of SN 2018zd (indicated by the tick marks). **(c)** Portion of an *HST* ACS/WFC F814W mosaic from 2004 April 10; the SN site is similarly indicated by tick marks. This mosaic consists of a single exposure, so to remove a number of cosmic-ray hits in the image, we use a masked mean filter to smooth any pixels that have a score of 0.001 or higher from our deep learning model (see Methods). The pixels associated with the progenitor candidate had scores $< 4 \times 10^{-5}$, so are not affected. **(d)** Same as panel (c), but with F658N on the same epoch. **(e)** Portion of a *Spitzer* IRAC 3.6 μm mosaic obtained on 2011 November 15, with the SN site again indicated by tick marks. All

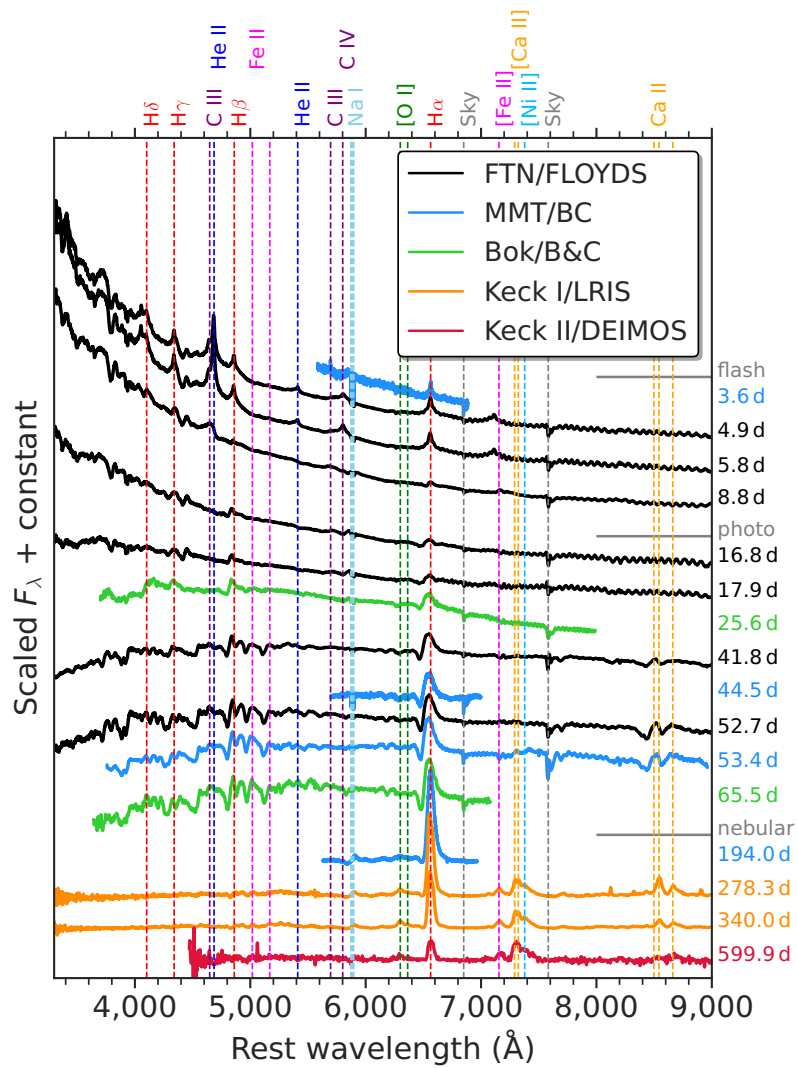
panels (b)–(e) are shown to the same scale and orientation, with north up and east to the left. The progenitor candidate is identified only in the single *HST* ACS/WFC F814W image (c).



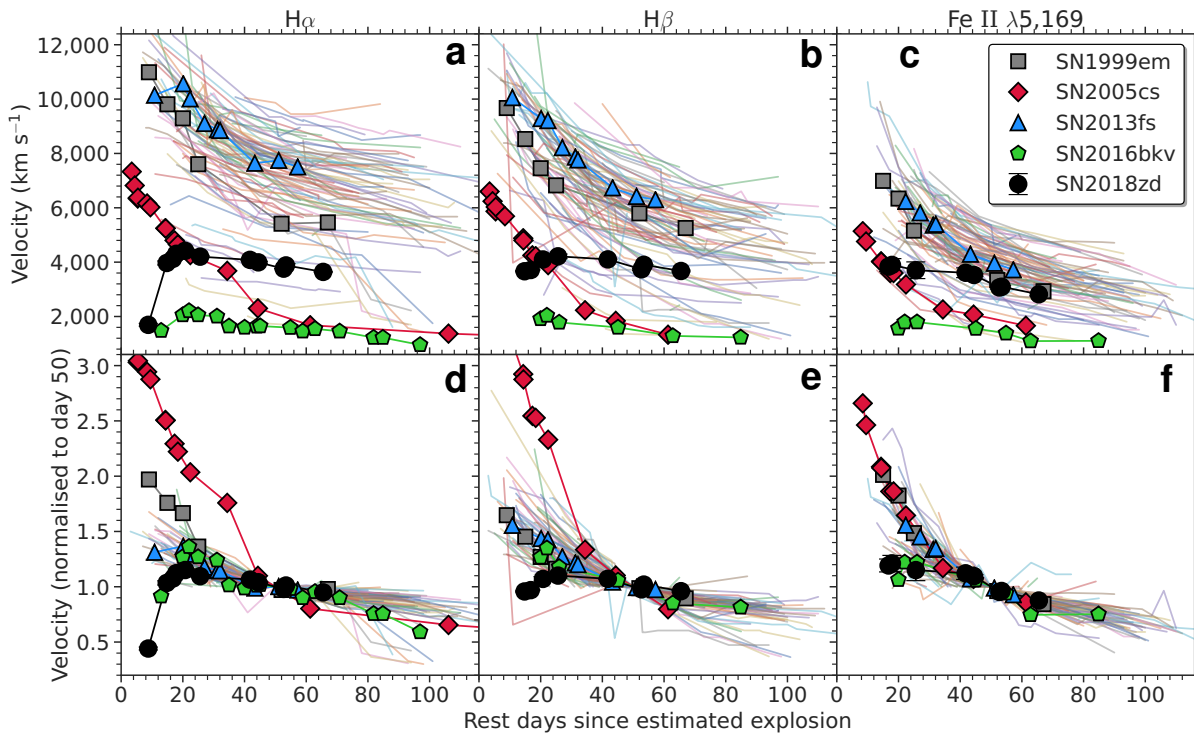
Extended Data Figure 2 SN progenitor and SAGB candidate SEDs. The SED for the SN 2018zd progenitor candidate resulting from pre-explosion *HST* and *Spitzer* archival data (black solid circles). For comparison we show model SEDs from BPASS v2.2⁹¹ for SAGB stars (navy curves), RSG stars at $M_{\text{init}} = 8 M_{\odot}$ (purple curves), and RSG stars at $M_{\text{init}} = 15 M_{\odot}$ (orange curves), at metallicities $Z = 0.02$ (short-dashed line) and $Z = 0.01$ (long-dashed line). Also shown for comparison is the SED for the SAGB candidate MSX SMC 055 (red open pentagons⁹³) and for the progenitor of the low-luminosity Type II-P SN 2005cs in M51 (blue open squares⁹⁵, green open diamonds⁹⁶). The luminosity of the *HST* ACS/WFC F814W detection of the SN 2018zd progenitor candidate lies between MSX SMC 055 and the SN 2005cs progenitor.



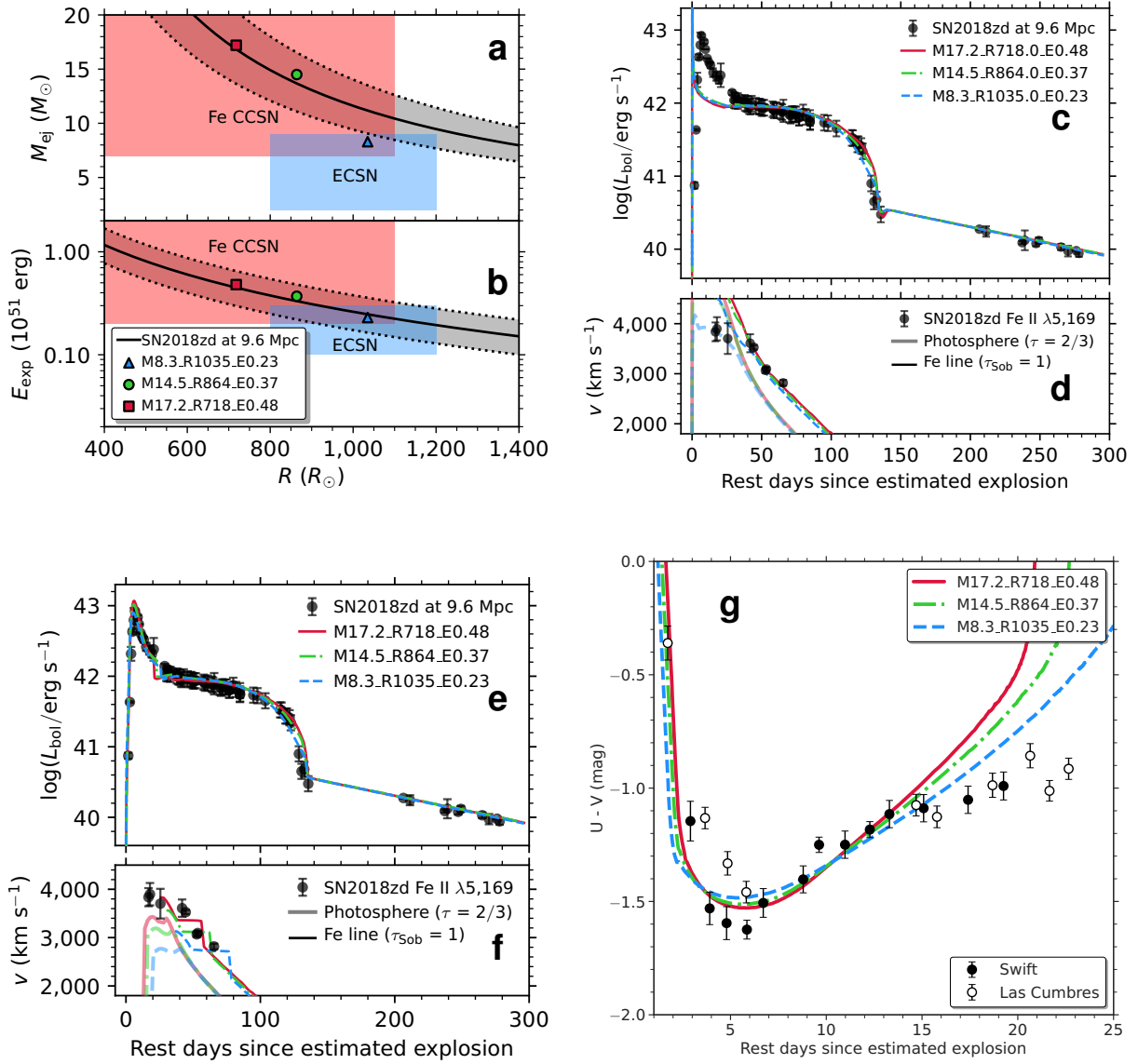
Extended Data Figure 3 Multiband light curve of SN 2018zd. (a) Multiband light curve of SN 2018zd focusing on the early rise. A quadratic function $F_1(t - t_0)^2$ is fitted to the unfiltered optical Itagaki and the first three Noguchi points to estimate an explosion epoch $t_0 = \text{MJD } 58178.4 \pm 0.1$. The observed flash spectroscopy epochs (Extended Data Fig. 4) are marked by the vertical dashed lines. Note the sharper rise in the *Swift* *UVW2* than in the *V* and unfiltered photometry during the flash-spectroscopy epochs. (b) Multiband light curve of SN 2018zd up to the ^{56}Co decay tail. The data gap is due to the Sun constraint. Error bars denote 1σ uncertainties and are sometimes smaller than the marker size. The light-curve shape resembles a typical Type II-P SN¹⁵¹. Comparing the luminosity on the tail to that of SN 1987A¹⁵², we estimate a ^{56}Ni mass of $(8.6 \pm 0.5) \times 10^{-3} M_{\odot}$ at the assumed luminosity distance of 9.6 Mpc.



Extended Data Figure 4 Optical spectral time series of SN 2018zd. The flash features (e.g., He II, C III, and C IV) persist up to > 8.8 d and disappear before 16.8 d. Then the broad Balmer-series P-Cygni lines appear, typical of the photospheric phase of a Type II-P SN¹⁵¹. After ~ 200 d, the nebular emission lines (e.g., H α , [Ca II], and [Ni II]) dominate over the relatively flat continuum.

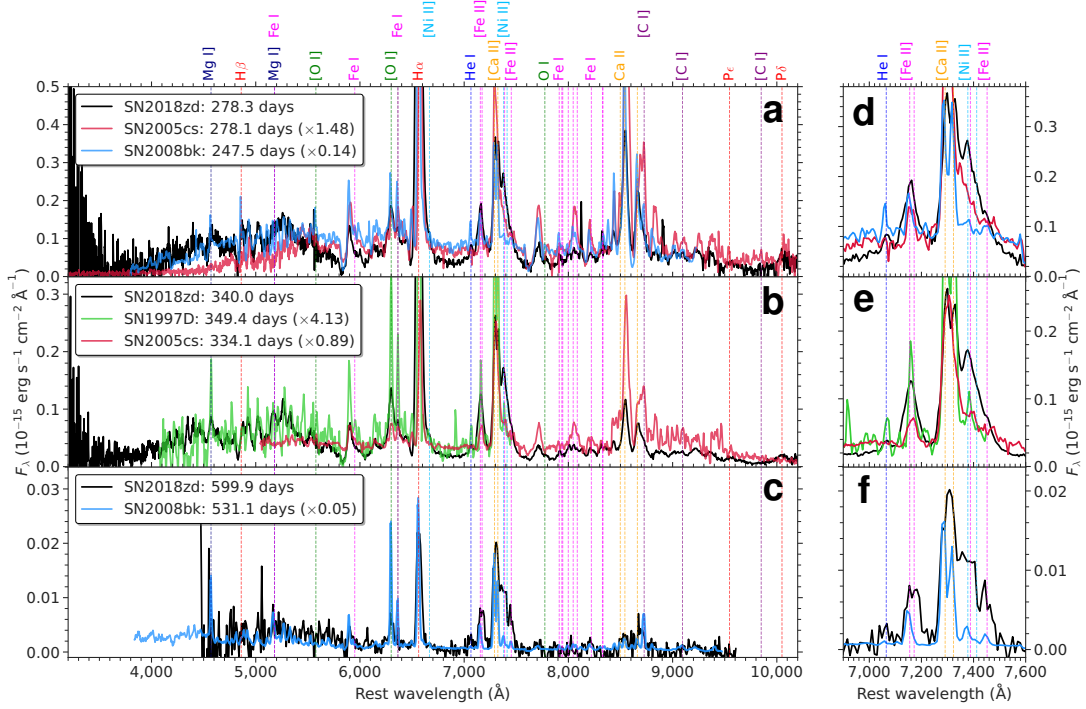


Extended Data Figure 5 Expansion velocities as a function of time. Comparison of the unnormalised (**a, b, c**) and normalised (to day 50; **d, e, f**) $H\alpha$, $H\beta$, and $\text{Fe II } \lambda 5169$ expansion velocities of SN 2018zd with a Type II SN sample¹⁵³ (transparent lines), including archetypal SN 1999em, along with low-luminosity SN 2005cs¹⁵⁴, early-flash SN 2013fs²¹, and low-luminosity and early-flash SN 2016bkv^{38, 155}. Error bars denote 1σ uncertainties and are sometimes smaller than the marker size. Note the pronounced early $H\alpha$ and $H\beta$ rises and the relatively flat velocity evolution (up to ~ 30 d) of SN 2018zd, indicating shock propagation inside the dense, optically-thick CSM.

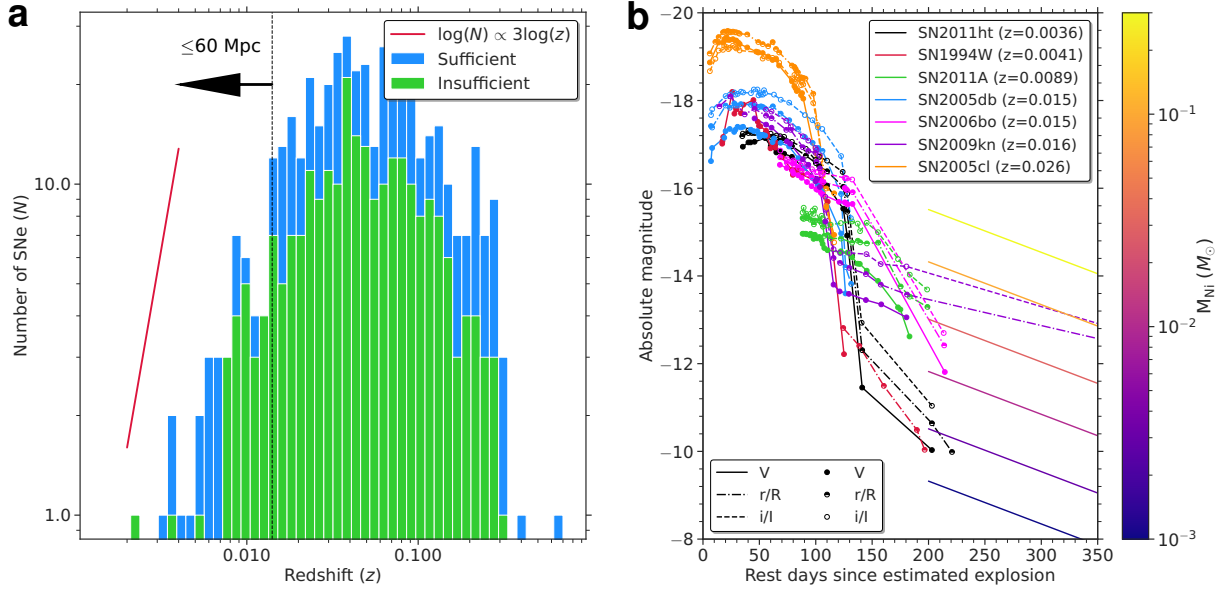


Extended Data Figure 6 MESA+STELLA progenitor and degenerate light-curve models. (a, b) Ejecta mass M_{ej} and explosion energy E_{exp} inferred from Eq. 1 as a function of progenitor radius R consistent with the bolometric light curve of SN 2018zd at the assumed luminosity distance of 9.6 ± 1.0 Mpc, along with the properties of the three degenerate explosion models. The blue and red shaded regions show explosion parameters expected for ECSNe^{9, 5, 6} and typical of Fe CCSNe¹⁵⁶, respectively. (c, d) Three degenerate MESA+STELLA explosion models providing good

fits to the light curve and velocities inferred from the Fe II $\lambda 5169$ line during the plateau phase. Models are labeled by $M[M_{\text{ej},\odot}]$ - $R[R_{\odot}]$ - $E[E_{\text{exp},51}]$. Error bars denote 1σ uncertainties. Note the observed early-time excess luminosity and suppressed velocity of SN 2018zd. This light-curve degeneracy highlights the inability to distinguish ECSNe from Fe CCSNe solely based on their light curves, suggesting that many ECSNe might have been overlooked owing to the lack of additional observations. **(e, f)** Same as panels (c, d), but adding a dense wind profile ($\dot{M}_{\text{wind}} = 0.01 M_{\odot} \text{ yr}^{-1}$, $v_{\text{wind}} = 20 \text{ km s}^{-1}$, and $t_{\text{wind}} = 10 \text{ yr}$) to the three degenerate MESA models before handoff to STELLA. **(g)** Comparison of the UV-colour models with the same wind CSM parameters as in panels (e, f). Error bars denote 1σ uncertainties. All three models with same wind CSM parameters are able to reproduce the early-time luminosity excess and blueward UV colour evolution almost identically, suggesting the insensitivity of a particular model choice. Despite a possible artificial velocity kink when the Fe line-forming region transitions from the CSM to the stellar ejecta, the velocity evolution with the early suppression is also reproduced.

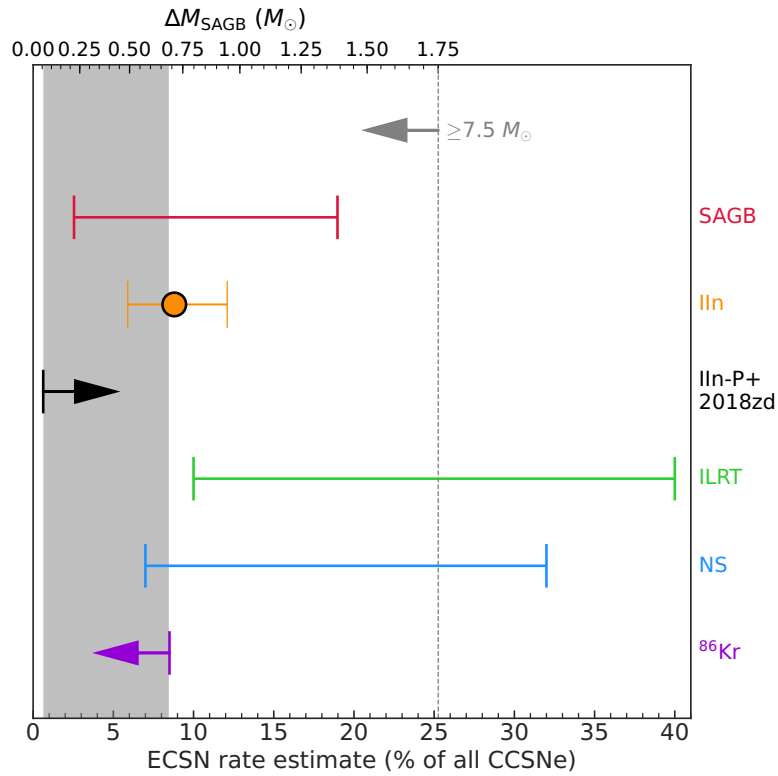


Extended Data Figure 7 Nebular spectral time series of low-luminosity Type II-P SNe. (a, b, c) Comparison of the nebular spectral time series of SN 2018zd with the scaled (by integrated flux as in the legend) and resampled low-luminosity Type II-P SNe 1997D¹⁵⁷, 2005cs¹⁵⁴, and 2008bk^{158, 159, 153}. In ascending order of wavelength, note the distinct Mg I] λ 4571 and [O I] λ 6300, 6364 + Fe I λ 6364 observed in SN 1997D; Fe I cluster 7900–8500 Å, [C I] λ 8727, and [C I] λ 9100 observed in SN 2005cs; and Mg I] λ 4571, [O I] λ 6300, 6364 + Fe I λ 6364, Fe I cluster 7900–8500 Å, and [C I] λ 8727 observed in SN 2008bk. **(d, e, f)** Same as panels (a, b, c), but zoomed into the wavelength range of interest (as in Fig. 4). Note the line intensity ratios of [Ni II] λ 7378/[Fe II] λ 7155 < 1 observed in SNe 1997D, 2005cs, and 2008bk. The strong C, O, Mg, and/or Fe lines combined with the weak Ni lines observed in SNe 1997D, 2005cs, and 2008bk are inconsistent with the ECSN chemical composition and nucleosynthesis.



Extended Data Figure 8 Public Type IIIn and IIIn-P SN samples. **(a)** Redshift distribution of the 455 public Type IIIn SNe retrieved from WISerEP and/or TNS. 241 objects have insufficient public spectra and/or light curves to secure the Type IIIn classifications and/or to be identified as Type IIIn-P SNe, but are included in the sample so as not to overestimate the lower limit. The red line is the number density slope by assuming the volume term with the standard cosmology ($H_0 = 71.0 \text{ km s}^{-1} \text{ Mpc}^{-1}$, $\Omega_{\Lambda_0} = 0.7$, and $\Omega_{m_0} = 0.3$, giving $d_L \propto z$ for $z < 0.1$). The black dotted line is the distance cut ($\leq 60 \text{ Mpc}$) we apply to compare with the LOSS sample^{149, 150}. By comparing the number density slope to the sample histogram as a first-order estimation, the sample does not seem to suffer significantly from incompleteness within 60 Mpc. **(b)** Comparison of the identified Type IIIn-P SN candidates by applying the two light-curve criteria. The explosion epochs of SNe 2006bo and 2011A are not well constrained and can shift up to $\pm 64 \text{ d}$ and $\pm 85 \text{ d}$, respectively^{146, 147}. The colour-coded tails at 200–350 d are the expected V -band tails from the

fully trapped radioactive heating for a given ^{56}Ni mass¹⁵². The observed Ni-mass upper limits are within 10^{-3} – $3 \times 10^{-2} M_{\odot}$ assuming that the tails are purely powered by the radioactive heating.



Extended Data Figure 9 ECSN rate estimators. Comparison of the ECSN rate estimates: “SAGB” is the SAGB mass window from stellar evolutionary calculations at solar metallicity⁴; “IIn” is the observed Type IIn SN rate from a volume-limited (≤ 60 Mpc) sample¹⁵⁰; “IIn-P+2018zd” is a rough lower limit of the Type IIn-P SN rate within 60 Mpc combined with SN 2018zd (see Methods); “ILRT” is a rough estimate from ILRTs within 30 Mpc¹²⁷; “NS” is an estimated rate from the bimodality in the neutron star mass distribution³⁶ assuming that the low-mass and high-mass peaks originate from ECSNe and Fe CCSNe, respectively; and “⁸⁶Kr” is an upper limit from the ECSN nucleosynthesis calculation¹¹³ assuming that ECSNe are the dominant production source of ⁸⁶Kr. The conversion between the fraction of all CCSNe and the SAGB mass window is performed assuming the Salpeter initial mass function with lower and upper CCSN mass limits of

$7.5 M_{\odot}^{124}$ and $120 M_{\odot}^{156}$ (respectively) and maximum and minimum SAGB masses of $9.25 M_{\odot}$ and $9.25 M_{\odot} - \Delta M_{\text{SAGB}}$ (respectively) at solar metallicity⁴. The grey vertical dotted line is where the minimum SAGB mass equals the assumed lower CCSN mass limit of $7.5 M_{\odot}$. The grey shaded region shows a rough ECSN rate constraint by the IIn-P+2018zd lower limit and the nucleosynthesis upper limit.

ECSN	Progenitor			Explosion		
Candidate	Identification	CSM	Chemical Composition	Energy	Light Curve	Nucleosynthesis
SN 2018zd	✓?	✓	✓	✓?	✓	✓
SN 1054 (Crab)	–	✓?	✓	✓	✓?	✓
ILRT	✓?	✓	?	×	×	?
Low-Lum. II-P	×	?	×	✓?	✓	×
IIn-P	?	✓	?	✓?	✓	✓?

Extended Data Table 1 ECSN candidate checklist. Check marks, check+question marks, and cross marks (respectively) indicate observations consistent, maybe consistent, and inconsistent with theoretical expectations. Dashed lines indicate the lack of observational constraints, and lone question marks indicate unknowns. For SN 2018zd, we identify a faint progenitor candidate that may be consistent with an SAGB star (Extended Data Figs. 1 & 2), and the explosion energy is consistent within the light curve degeneracy (Extended Data Fig. 6). For low-luminosity Type II-P SNe and Type IIn-P SNe, the overall light-curve morphology can be reproduced within the expected explosion energy range^{7, 8, 18, 120}. For Type IIn-P SN 2011ht¹⁶⁰, we measure $[\text{Ni II}] \lambda 7378 / [\text{Fe II}] \lambda 7155 = 3.8$ at 155 d after the explosion, which may indicate ECSN-like nucleosynthesis, although the spectrum may not be fully nebular given the relatively early phase.